https://doi.org/10.5194/egusphere-2026-1054
Preprint. Discussion started: 4 May 2026

Evolution mechanisms of explosive advection sea fog under the influence of transported dust aerosol: a case study over the East China Sea in spring 2025

Xirui Ma[1,2,3], Yun Zhang[2,3], Panyan Ge[1,2,3], Yan Yin[1], Hepeng Zheng[2,3], Tingting Kang[2,3], Lingbing Bu[1], Wenjie Su[2,3], Donglin Yang[2,3], Qiangyue Xiang[2,3], Yinze Ran[4,5]

[1]Key Laboratory for Aerosol-Cloud-Precipitation of China Meteorological Administration/Collaborative Innovation Centre on Forecast and Evaluation of Meteorological Disasters (CIC-FEMD), Nanjing University of Information Science & Technology, Nanjing 210044, China
[2]College of Meteorology and Oceanography, National University of Defense Technology, Changsha 410073, China
[3]High Impact Weather Key Laboratory of CMA, Changsha 410073, China
[4]Key Laboratory of Physical Oceanography, Ocean University of China, Qingdao 266000, China
[5]College of Oceanic and Atmospheric Sciences, Ocean University of China, Qingdao 266000, China

Correspondence to: Yun Zhang (zhangyun.1207@163.com)

Abstract. Evolution mechanisms of explosive advection sea fog coupled with long-range dust transport over East Asia remain unclear. This study investigates a dust-advection sea fog event using multi-source data. Results show that dust underwent significant aging during transport, promoting sea fog under high humidity (RH > 90%). Before sea fog formation (Stage 3: 12:40-16:47 on the 25th) and during the sea fog period (Stage 4: 16:47-19:30 on the 25th), the proportion of 0-1 μm particles decreased by 18% and 24%, respectively. The proportion of 1-2.5 μm particles increased by 5% and 4%, respectively. The proportion of 2.5-10 μm particles increased by 13% and 20%, respectively. This indicates that aging enhanced dust hygroscopicity. Unlike classical advection cooling, radiative forcing of dust and cold air formed a deep inversion (9°C) before fog, which with warm-moist advection suppressed turbulent mixing and provided a favourable thermodynamic background for fog maintenance. The threshold ranges of turbulence parameters (U, TKE, u_*, I_u, I_v, I_w) were relatively distinct when sea fog maintains visibility within 1 km. The friction velocity (u_*) was within a narrow range of 0.62–0.69 ms^{-1}, indicating high sensitivity to u_*. The system showed a significant characteristic of turbulence acting first and fog responding later during the late stage of mist. The downward longwave radiation (DLR) was highly sensitive to changes in fog layer structure. Fog dissipation was caused by circulation adjustment and re-invasion of dry-cold dust carried by northerly winds, destroying phase equilibrium. These findings advance understanding of sea fog under complex aerosol backgrounds.

1 Introduction

Fog is a hazardous weather phenomenon that occurs at the bottom of the planetary boundary layer. It essentially consists of tiny water droplets or ice crystals suspended in the near-surface atmosphere, leading to low horizontal visibility (Gultepe et

https://doi.org/10.5194/egusphere-2026-1054
Preprint. Discussion started: 4 May 2026

al., 2007). Its low visibility has serious impacts on transportation, aviation, power systems, and human health (Gultepe et al., 2015; Niu et al., 2010a). Most observational and simulation studies mainly focus on land radiation fog (Fernando et al., 2021; Gultepe et al., 2014; Liu et al., 2011; Ian et al., 2018; Brege et al., 2018; Jia et al., 2019; Tsai et al., 2021), while relatively fewer studies pay attention to sea fog. Sea fog is usually formed by advection cooling when warm-moist air masses flow over cold ocean surfaces (Cotton et al., 1989; Gilson et al., 2018). The life cycle of sea fog is controlled by more complex physical processes. It is the result of nonlinear coupling of aerosol activation, condensation, radiation, turbulence, thermodynamic and dynamic processes at multiple scales (Mazoyer et al., 2017; Tardif et al., 2007; Haeffelin et al., 2010). These processes interact with each other in complex ways. Currently, the understanding of sea fog mechanisms remains insufficient, and accurate prediction of sea fog still has significant uncertainty. Therefore, advancing a comprehensive understanding of the microphysical processes of sea fog is crucial (Yang and Gao, 2020).

Atmospheric aerosols play an important role in global climate by affecting the Earth-atmosphere radiation balance through direct or indirect effects (Huang et al., 2014; Bellouin et al., 2020; Liu et al., 2021). The interaction between aerosols and fog is rather complex and has similarities with the interaction between aerosols and clouds (Fan et al., 2016; Guo et al., 2018; Wang et al., 2023). As cloud condensation nuclei (CCN) (Twomey 1959), the concentration, size, and chemical composition of aerosols can significantly affect the microphysical and optical properties of fog (Jia et al., 2019; Yan et al., 2020; Dusek et al., 2006; Zhao and Garrett, 2015). Meanwhile, fog processes can also modify the evolution of aerosols (such as size, composition, mixing state, new particle formation, wet scavenging, etc.) (Schroder et al., 2015; Qian et al., 2023; Roth et al., 2016; Biswas et al., 2008). Numerous studies have shown that the increase in aerosol concentration can lead to higher fog droplet number concentration (Liu et al., 2021; Yan et al., 2020; Maalick et al., 2016; Stolaki et al., 2015) and fog top height (Liu et al., 2021; Stolaki et al., 2015), and may extend the fog lifetime (Quan et al., 2021; Yan et al., 2021). Currently, research on the interaction between sea fog and aerosols is still limited. Previous studies have mostly focused on sea salt aerosols acting as condensation nuclei for sea fog. However, spring is both the outbreak period of sea fog and dust. Studies have shown that dust from northern China and Mongolia can be transported over long distances across the Yellow Sea, East Sea, and even to the Pacific Ocean (Cahill et al., 2003; Sullivan et al., 2007). Traditional views suggest that pure dust is hydrophobic (Li et al., 2025) and tends to inhibit fog formation. Dust can undergo atmospheric aging through coagulation, cloud processes, and heterogeneous chemical reactions on surfaces. It can mix with ammonium sulfate, ammonium nitrate, and biomass burning particles (Li et al., 2025; Clarke et al., 2004; Korhonen et al., 2003; Yin et al., 2002; Zhang and Iwasaka, 2004; Zhang et al., 2003). It can also react with marine biogenic DMS to promote sulfate formation, thus forming complex internal mixing states (Zhuang et al., 1992; Zhang et al., 2000). Studies have indicated that long-range transported dust undergoes aging processes, and its hygroscopicity is significantly enhanced (Li et al., 2025; Tobo et al., 2010; Sullivan et al., 2009; Ma et al., 2013; Yin et al., 2007). Due to the very complex interactions of multiple influencing factors between long-range transported dust and sea fog, the details of the effects of long-range transported dust on sea fog processes have not been well understood.

https://doi.org/10.5194/egusphere-2026-1054
Preprint. Discussion started: 4 May 2026

The radiative forcing of aerosols can alter the thermodynamic and dynamic structure of the boundary layer (Deaconu et al., 2019; De Graaf et al., 2020), which can change the formation and dissipation conditions as well as the life cycle of fog. The strong scattering and absorption of shortwave radiation by dust aerosols can cause significant cooling of near-surface atmosphere (Obiso et al., 2024; Wang et al., 2024). For advection sea fog, the classical theory mainly emphasizes the advection cooling mechanism when warm-moist air flows over cold sea surfaces (Yang et al., 2024). However, under dusty conditions, can the radiative cooling induced by the aerosol layer promote the establishment of an inversion layer? There is still a lack of sufficient understanding. Inversion can provide stable stratification conditions for fog formation (Fitzjarrald and Lala, 1989; Holets and Swanson, 1981; Roach et al., 1976). Currently, research on the feedback mechanism between aerosol radiative effects and boundary layer thermal stratification has mostly focused on heavy pollution and haze processes over land. The role in marine advection fog remains unclear. In fact, radiation is a key factor regulating the life cycle of sea fog (Fernando et al., 2021; Yun and Ha, 2022). In addition, observational and simulation studies have indicated that turbulence can affect the macrophysics of fog (Ye and Zhang, 2015; Porson et al., 2011) (suppressing or deepening the fog top height (Zhou and Ferrier, 2008)). However, moderate turbulence can promote fog development (Zhou and Ferrier, 2008; Price, 2019). Turbulence that is too weak is unfavourable for water vapor transport, while turbulence that is too strong leads to air entrainment and dissipation. Under the high aerosol background caused by the explosive input of dust, is there a moderate turbulence threshold for maintaining sea fog? The microphysical evolution and dynamic processes during sea fog do not exist in isolation. Their realization is inevitably controlled by the macroscale modulation of synoptic conditions and sea-air interface conditions (Yang et al., 2024; Dorman et al., 2021).

Previous sea fog research has mostly focused on long-term statistical characteristic analysis. However, systematic case study analysis is still lacking for the refined physical mechanisms of the full life cycle of sea fog under complex synoptic backgrounds, especially during dust aerosol intrusion. How do aerosols, radiation, turbulence, synoptic, and air-sea conditions co-evolve in this complex coupling process? Do dust aerosols promote or inhibit sea fog formation? How does the aerosol-radiation-turbulence feedback mechanism affect the life cycle of sea fog? Is there a specific turbulence dynamics threshold during sea fog periods? To address the scientific questions, this paper utilized multi-source data including Himawari-9 satellite remote sensing data, relevant data from the ground observation platform at Qingbang Island in the East China Sea, and ERA5 reanalysis, to conduct a full life-cycle study of a event of explosive dust transport and advection sea fog coupling that occurred from March 24 to 28, 2025. The aim of this study is to clarify the comprehensive driving mechanism of sea fog formation and dissipation in the dust aerosol environment by exploring the evolution laws of aerosol microphysics, radiation and boundary layer thermodynamic structure, turbulent dynamic characteristics, as well as synoptic conditions and air-sea conditions during this event. The organizational structure of this paper is as follows: Section 2 introduces the observation site, data sources and analysis methods. Section 3 systematically presents the results and discussions. The focus is on analysing the comprehensive influence of the physicochemical properties of aerosols, radiation characteristics and feedback of boundary layer thermodynamic structure, turbulent dynamic characteristics, and multi-scale meteorological conditions during the sea fog process. Section 4 summarizes the main conclusions.

https://doi.org/10.5194/egusphere-2026-1054
Preprint. Discussion started: 4 May 2026

2 Materials and methods

2.1 Observation period and regions

The study area is located at Qingbang Island (30.1°N, 122.4°E) in the East China Sea. The observation instruments were deployed at Xifeng Bay on this island. The geographical location is shown in Figure 1. This island belongs to the Zhoushan Archipelago and is far from land. It is less affected by direct interference from anthropogenic emission sources on land and can well represent the typical marine atmospheric background environment of the East China Sea. This sea area is a high-incidence region of advection sea fog. Sea fog phenomena are significantly concentrated in spring (March to May). Currently, sea fog observation data in the East China Sea are relatively limited and observation is difficult. This study utilized the unique geographical advantage of Qingbang Island to conduct fixed-point observations. The aim is to further understand the refined evolution process of sea fog. A dust-advection sea fog case observed from March 24 to 28, 2025 was selected to explore the multi-scale comprehensive mechanism of sea fog processes under complex environmental conditions.

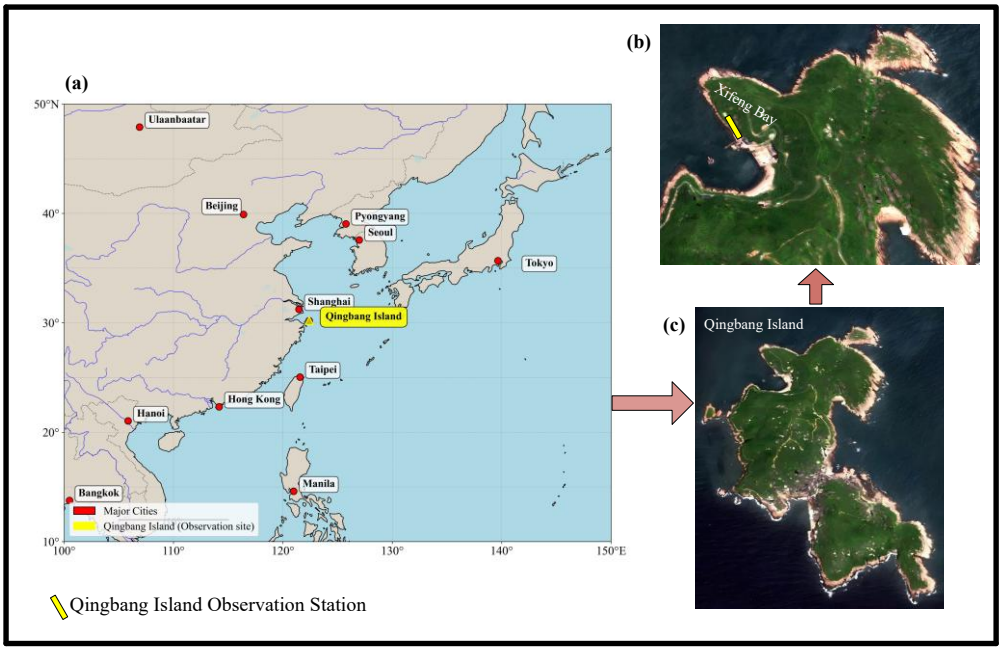

Figure 1: Geographical location of the observation site. The satellite images in panels (b) and (c) are from © Google Earth.

2.1 Instruments and data analysis

The data used during the study period mainly include: (1) surface meteorological observation data; (2) radiation data; (3) near-surface turbulence observation data; (4) microwave radiometer retrieval data; (5) Himawari-9 satellite data(https://www.eorc.jaxa.jp/ptree/index.html); (6) ERA5 reanalysis data(https://cds.climate.copernicus.eu/). The data sources and instrument descriptions are shown in Table 1.

Table 1. List of data sources and instruments.

https://doi.org/10.5194/egusphere-2026-1054
Preprint. Discussion started: 4 May 2026

Data category	Instruments	Measurement parameters	Range/Accuracy	Interval
Weather Station data	AWS1900 Automatic Weather Station	T	-30-70 ℃ ± 0.1 ℃	10s
		RH	0-100% ± 2.5%	
		P_a	450-1100 hPa ± 0.1 hPa	
		WS	0.5-65 ms^{-1} ± 0.5 ms^{-1}	
		WD	0-360° ± 2°	
		PM	0-999 ugm^{-3} ± 10 ugm^{-3}	
		Vis	10-10000 m ± 5%	
Radiation data	CNR4-KIPZONE	DSR, USR, DLR, ULR	0-2000 Wm^{-2} ± 5%	1min
Turbulence data	CSAT3	u, v, w	± 0.04 ms^{-1} for horizontal ± 0.02 ms^{-1} for Vertical	10Hz
Microwave radiometer data	RPG-HATPRO	T	0-10 km	10s
Satellite data	Himawari-9	AOD	5 km	1h
		$BT_{3.89}$, $BT_{11.24}$	2 km	10min
Reanalysis data	ERA5(ECMWF)	MSLP, T_{2m}, u_{10m}, v_{10m} SST, Z_{850} d_{2m}	0.25°×0.25°	1h

Due to the lack of conventional meteorological data with high spatiotemporal resolution in this sea area, raw observation data with a temporal resolution of 10 s were obtained by the automatic weather station (AWS) independently established in this study. The main observation parameters include air temperature (T), relative humidity (RH), pressure (Pa), wind speed (WS), wind direction (WD), particulate matter mass concentration (PM_1、$PM_{2.5}$、PM_{10}), and visibility (Vis). To eliminate high-frequency random noise and ensure data stability, all surface meteorological elements were subjected to strict quality control and were averaged into time series data with 1 min intervals for subsequent analysis.

Radiation parameters were measured by a four-component radiometer (CNR4). This instrument can simultaneously measure downward shortwave radiation (DSR), upward shortwave radiation (USR), downward longwave radiation (DLR), and upward longwave radiation (ULR). Net radiation (Rn) was calculated based on the surface radiation balance equation: Rn = (DSR - USR) + (DLR - ULR). To match the analysis scale of boundary layer fluxes, all radiation component data were processed into 30-min averages. In addition, a ground-based microwave radiometer (RPG-HATPRO) was used. Vertical profiles of air temperature in the boundary layer with high temporal resolution were obtained through retrieval algorithms.

In this study, a 3-D Sonic Anemometer (CSAT3) was used for near-surface turbulence observation. It can measure instantaneous 3-D wind velocities (u, v, w) and sonic speed (c). The acoustic virtual temperature (Tv) was calculated from these measurements. The processing of turbulence data mainly included outlier removal, strict quality control, planar fit rotation, damping loss correction, and Webb-Pearman-Leuning (WPL) correction (Schaller et al., 2017).

https://doi.org/10.5194/egusphere-2026-1054
Preprint. Discussion started: 4 May 2026

For large-scale monitoring, L1 data from Himawari-9 (H-9), the new-generation geostationary meteorological satellite of the Japan Meteorological Agency (JMA), was used in this study. The satellite is equipped with the Advanced Himawari Imager (AHI), which has the capability of high-frequency and multi-spectral observations (Bessho et al., 2016). For fog area identification, the commonly used steps in fog detection were combined, including temperature, texture, and noise monitoring. Nighttime fog was identified based on the brightness temperature difference (BT3.89–BT11.24) between the mid-infrared channel at 3.89 μm and the thermal infrared channel at 11.24 μm (Kim et al., 2019). For aerosol optical depth (AOD) data, the AHI L3 gridded aerosol product provided by JAXA Himawari Monitor (supported by the MASINGAR model system) was used. This product constrains the Meteorological Research Institute (MRI) aerosol transport model by assimilating AOD retrieved from H-9. Hourly AOD for components including sulfate, organic carbon, black carbon, sea salt, and dust can be output. During sea fog occurrences, satellite retrievals may be filtered out or contaminated by cloud screening mechanisms. In this case, model outputs lack direct observational constraints. Therefore, during sea fog occurrences, this AOD data was mainly used as a qualitative or semi-quantitative reference for the regional background aerosol environment. It was not used as an accurate observational basis for aerosol microphysical changes within the fog.

Finally, to clarify the background circulation pattern and air-sea conditions of this dust-sea fog event, ERA5 reanalysis data provided by the European Centre for Medium-Range Weather Forecasts (ECMWF) was used in this study (Yang et al., 2024). The extracted variables include mean sea level pressure (MSLP), 2-m air temperature (T2m), 2-m dew point temperature (d2m), sea surface temperature (SST), 10-m wind speed (u10m, v10m), and 850 hPa geopotential height (Z850).

2.2 Methods

The aerosol mass extinction efficiency (MEE) is a key parameter for characterizing the optical properties of aerosols. Its physical meaning is the scattering and absorption efficiency of light by particles with a unit mass concentration. It directly reflects the attenuation ability of aerosols on atmospheric visibility (Saide et al., 2022). Due to the lack of liquid water content data in this study, the MEE is defined as the ratio of the aerosol extinction coefficient (σ_{ext}) to the aerosol mass concentration:

$$\mathrm{MEE} = \sigma_{ext} / \rho(\mathrm{PM}_{2.5}) \quad (1)$$

$$\sigma_{ext} = 3921/\mathrm{Vis} \quad (2)$$

Where σ_{ext} is the aerosol extinction coefficient with a unit of Mm^{-1}, $\rho(PM_{2.5})$ is the mass concentration of $PM_{2.5}$ with a unit of $\mu g \cdot m^{-3}$, the unit of Vis is km, and 3.912 is the Koschmeider constant (Lee and Shang, 2016).

In order to study the evolution characteristics of turbulence during this event, high-frequency fluctuation data obtained from the 3-D Sonic Anemometer (CSAT3) was used. Turbulence-related parameters were calculated using the eddy covariance method (Zhou and Ferrier, 2008). These include turbulence intensity (I_u, I_v, I_w), horizontal mean wind speed (U), friction velocity (u_*), turbulent kinetic energy (TKE), and stability parameter (ζ). The calculation expressions of related physical quantities are as follows:

https://doi.org/10.5194/egusphere-2026-1054
Preprint. Discussion started: 4 May 2026

$$I_u = \sigma_u / U \quad I_v = \sigma_u / U \quad I_z = \sigma_u / U \tag{3}$$

$$\sigma_u = \sqrt{\overline{u'^2}} \quad \sigma_v = \sqrt{\overline{v'^2}} \quad \sigma_z = \sqrt{\overline{z'^2}} \tag{4}$$

$$u_* = \left(\overline{u'w'^2} + \overline{v'w'^2}\right)^{1/4} \tag{5}$$

$$TKE = \frac{1}{2}\left(\overline{u'^2} + \overline{v'^2} + \overline{w'^2}\right) \tag{6}$$

$$\zeta = z/L \tag{7}$$

Where u', v', w' are the wind velocity fluctuations of u, v, w. σ_u, σ_v, σ_w are the standard deviations of wind velocity, z is the instrument observation height, and L is the Monin-Obukhov length.

3 Results and discussion

3.1 Overview of dust-sea Fog events

During March 24–28, 2025, the Qingbang Island in the East China Sea experienced an event of dust -advection sea fog. This process was clearly monitored by the H-9 satellite (Fig. 2).

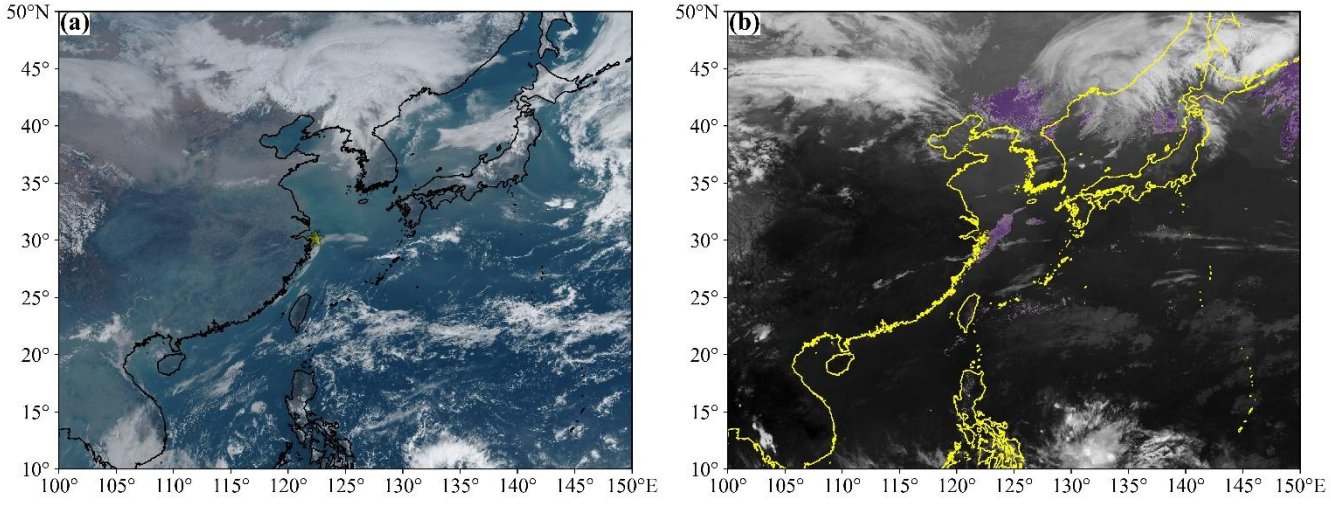

https://doi.org/10.5194/egusphere-2026-1054
Preprint. Discussion started: 4 May 2026

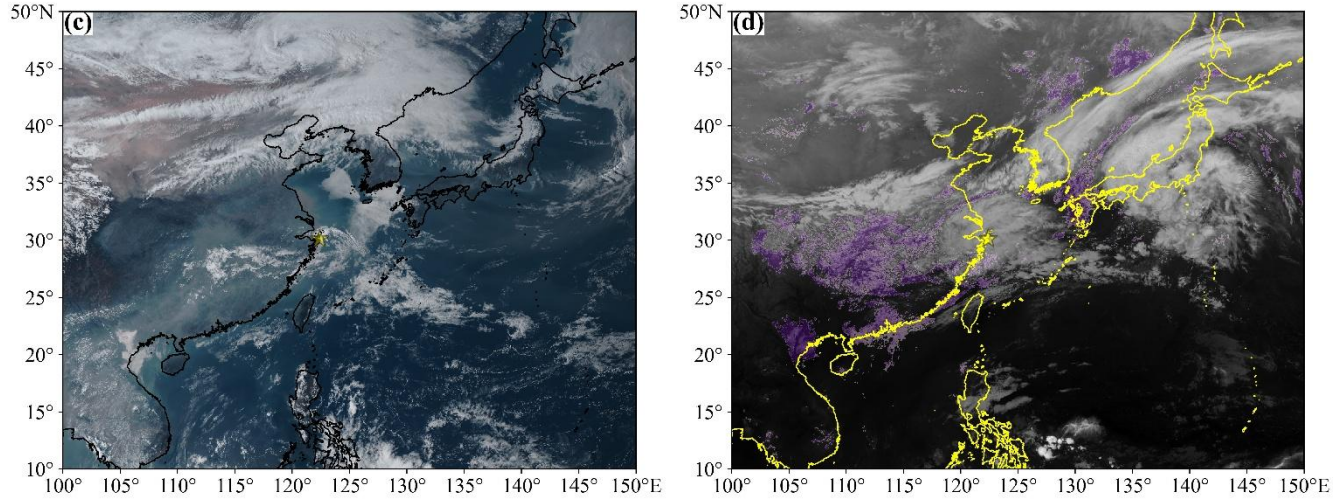

Figure 2: Sea fog monitoring images from the H-9 satellite. (a, c are the AHI RGB true-colour images at 09:00 LST on March 25 and 15:00 LST on March 26, respectively (local standard time (LST) = Universal Time Coordinated (UTC) + 8 h). b, d are the sea fog identification images at 18:00 LST on March 25 and 00:00 LST on March 28, respectively. Purple indicates fog identified at nighttime. The yellow pentagram indicates the observation site.)

The satellite monitoring results showed that at 09:00 LST on March 25 (Fig. 2(a)), sea fog first formed in the coastal area with a hook-shaped distribution. It was close to but did not cover the observation site. In the AHI RGB true-color images, the fog area appeared as gray and uniform features compared to the surrounding clouds. This is consistent with the typical radiative characteristics of sea fog (Lv et al., 2014). Subsequently, the sea fog system showed obvious offshore development and expansion. By 18:00 LST on March 25 (Fig. 2(b)), the fog area had expanded to the observation site. Its main body evolved into an elongated columnar structure. Its range extended to the central Yellow Sea, indicating that the sea fog had entered a mature development stage. At 15:00 LST on March 26 (Fig. 2(c)), the morphology and structure of the sea fog changed significantly. The previously continuous fog belt began to show fragmented and discrete distribution, and the overall structure weakened. This indicates that the boundary layer conditions maintaining fog layer stability (such as low-level cooling or inversion structure) may have begun to weaken. Finally, at 00:00 LST on March 28 (Fig. 2(d)), the sea fog at the observation site had completely dissipated. The satellite sea fog monitoring results indicate that this sea fog event has similar spatial evolution characteristics to typical advection fog (Lv et al., 2014).

The satellite monitoring results provided the overall spatial structure and evolution characteristics of this advection fog event. To clarify the specific evolution processes of various meteorological elements and atmospheric particulate matter during this event, a comprehensive analysis was conducted based on ground observation data of meteorology and pollutants. Fig. 3 shows the temporal evolution characteristics of mass concentrations (PM_1, $PM_{2.5}$, PM_{10}), atmospheric visibility (Vis), and main meteorological elements (relative humidity (RH), temperature (T), pressure (Pa), wind speed (WS), and wind direction (WD)) during the observation period.

https://doi.org/10.5194/egusphere-2026-1054
Preprint. Discussion started: 4 May 2026

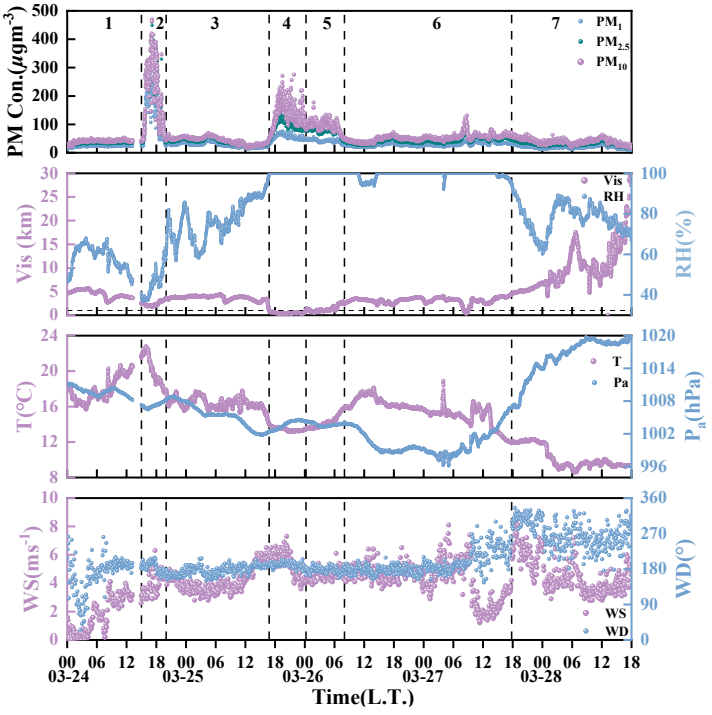

Figure 3: Pollutant concentrations and meteorological elements during the observation period.

Based on the fog identification criteria of WMO (WMO/GAW, 2003) and the UK Met Office (Met Office, 1994) (Vis < 1 km and RH ≥ 95% is identified as fog, 1 km ≤ Vis ＜ 5 km and RH ≥ 95% is identified as mist). This event was divided into 7 detailed stages (Table 2). Table 2 shows the sequence numbers, stage name, time, visibility, and relative humidity of the 7 stages.

Table 2. Seven refined phases of the event

Stages	Name	Time	Vis (km) (Average value)	RH (%)
1	Pre-dust phase	Mar 24 00:00-15:00	4.8-2.5 (4.5)	47-40
2	Dust phase	Mar 24 15:00-20:00	2.5-3.7 (2.4)	40-65
3	Pre-formation phase of advection sea fog	Mar 24 20:00-Mar 25 16:47	3.7-1 (3.7)	65-100
4	Advection sea fog phase	Mar 25 16:47-Mar 26 00:15	0-1 (0.4)	100
5	Alternating evolution phase of advection sea fog and mist	Mar 26 00:15-08:00	1-2.3 (1.2)	100
6	Sustaining phase of mist	Mar 26 08:00-Mar 27 17:47	2.3-4.5 (3.1)	100-95
7	Dissipation phase of mist	Mar 27 17:47-Mar 28 18:00	4.5-30 (10)	95-69

*The Vis and RH values (in the form of a_{t1}-b_{t2}) are the values corresponding to time t_1-t_2; Vis (Average value) is the average visibility value within this stage.

Fig. 3 shows that the mass concentrations of PM_1, $PM_{2.5}$, and PM_{10} were relatively stable during Stage 1. The average mass concentrations were 22, 33, and 41 μg/m³, respectively. The RH showed a trend of first increasing and then oscillating

https://doi.org/10.5194/egusphere-2026-1054
Preprint. Discussion started: 4 May 2026

downward due to the enhancement of solar radiation and dry air entrainment. The overall wind speed was below 4 m/s. The key feature of this stage was two wind direction changes. First, the west wind turned counterclockwise to north-northeast (NNE), bringing cold air intrusion with a temperature drop of 2.6°C. Then, the wind direction remained at south to south-southwest (S-SSW) after 08:00. This established the basic conditions for water vapor accumulation of advection sea fog.

Stage 2 was affected by strong external disturbance. The PM mass concentrations showed explosive increases during this period. The peak values of PM_1, $PM_{2.5}$, and PM_{10} at 17:08 on March 24 were 267, 460, and 469 μg/m³, respectively (an increase of 11-14 times). This trend is consistent with the explosive input characteristics of dust aerosols (Rodríguez et al., 2024). Therefore, this stage was inferred and defined as the dust passage period (supported by satellite data in Section 3.1). The radiative cooling effect of dust combined with cold air intrusion intensified the extent and rate of temperature drop (a decrease of 5.0°C within five hours, with a cooling rate of 1.0°C/h). The visibility dropped sharply by 28.4% to 1.79 km, showing a strict inverse trend with PM mass concentration changes. The near-synchronous coupling between the PM mass concentration peak (17:08) and the wind speed peak (6.3 m/s) might indicate the enhanced downward transport of dust aerosols by turbulent mixing during this stage. In addition, the pressure showed an increase during 16:27-20:00. This may be related to the thermodynamic pressurization effect of aerosol increase on the local boundary layer (Luo et al., 2022).

The system then entered the coupling period of the core mechanism of sea fog outbreak, including Stage 3 and Stage 4. At the beginning of Stage 3, the residual dust aerosols showed a gentle oscillating decrease. The settling rate of PM_{10} was about 1.8 μg/m³/h, which is consistent with the gravitational settling model. The PM mass concentrations increased during 12:32-16:47 on March 25. This may be related to the hygroscopic growth of aerosol particles. During 04:30-09:00 on March 25, the wind direction of near-surface changed from land to sea breeze. After 09:00 on March 25, the wind speed continued to increase to 6.0 $m \cdot s^{-1}$ with continuous warm and moist advection. This provided sufficient water vapor transport for sea fog outbreak. It was favourable for the hygroscopic growth of settled dust and other aerosols to prepare for sea fog outbreak. At the end of Stage 3 (16:20-16:47), the thermodynamic conditions changed obviously. The temperature cooling rate was about 2.89°C/h, and the RH jumped to 100%. At the same time, the pressure turned to a weak increase after reaching the bottom since 15:30 on March 25. This indicates that the overall environmental field (thermal and dynamic background) changed. The combined effect of thermal and dynamic condition changes finally led to a sharp decrease in visibility to 1.0 km at 16:47 on March 25. During Stage 4, the visibility decreased sharply. The minimum visibility was 0.31 km. The aerosol concentrations showed a significant increase with multi-peak fluctuation characteristics.

The system attenuation began in Stage 5, which was still under the conditions of RH at 100% and stable southerly wind. The PM mass concentrations showed a three-peak decreasing trend, and the decreasing rate showed $PM_{10} > PM_{2.5} > PM_1$. This was closely related to the efficient removal of coarse aerosol particles by the gravitational collision and wet deposition of fog droplets. The atmospheric visibility was basically maintained at about 1 km, consistent with the alternating evolution trend of advection sea fog and mist. In Stage 6, the stable southerly wind drove the RH to remain at 95%-100%. A dynamic balance was formed between warm and moist advection and highly hygroscopic aerosols. The mist state was maintained for 33 hours (visibility 2-4 km). A dense fog disturbance event of nearly 1 hour occurred during this stage. During 08:08-09:05

https://doi.org/10.5194/egusphere-2026-1054
Preprint. Discussion started: 4 May 2026

on March 27, PM_{10} suddenly increased to 131 μg/m³. The visibility dropped sharply to 0.4 km. The wind speed increased to 5.8 m/s. After 09:25 on March 27, the northwest wind intruded. The intrusion of dry and cold air caused significant cooling. The RH dropped to the critical value of 95%. This caused the mist system to collapse (visibility increased to 4 km).

In the final Stage 7, driven by the continuously strengthening of the northwest wind, the dry and cold air mass completely replaced the warm and moist marine air mass. This caused the RH to drop from 95% to 77%, breaking the phase transition critical value of aerosols. In the early period from 17:50 to 19:00 on March 27, the wind speed increased from 6.4 to 9 m/s. This enhanced the turbulent vertical mixing and mechanically destroyed the residual fog droplets. The average mass concentrations of PM_1, $PM_{2.5}$, and PM_{10} in this stage decreased by 30%, 28%, and 25%, respectively, compared to those in Stage 6. The visibility continued to increase to 30 km, indicating the irreversible dissipation of the mist system.

3.2 Analysis of Aerosol Characteristics

This analysis aimed to investigate whether the explosive increase of PM mass concentrations in Stage 2 was caused by dust transport passing through the observation site. It also explored whether dust had an impact on the evolution mechanism of sea fog. The AOD data of different aerosol types from H-9 were used. The distribution results of different aerosol types in different regions at typical moments during this event (Fig. 4).

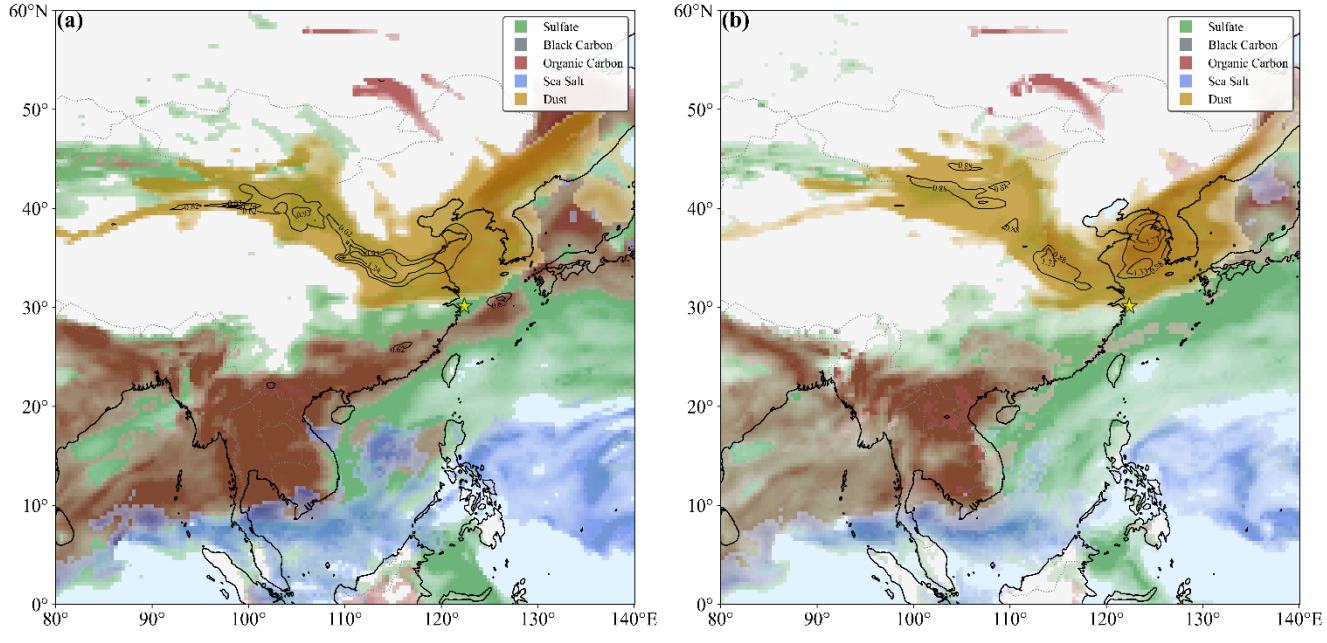

https://doi.org/10.5194/egusphere-2026-1054
Preprint. Discussion started: 4 May 2026

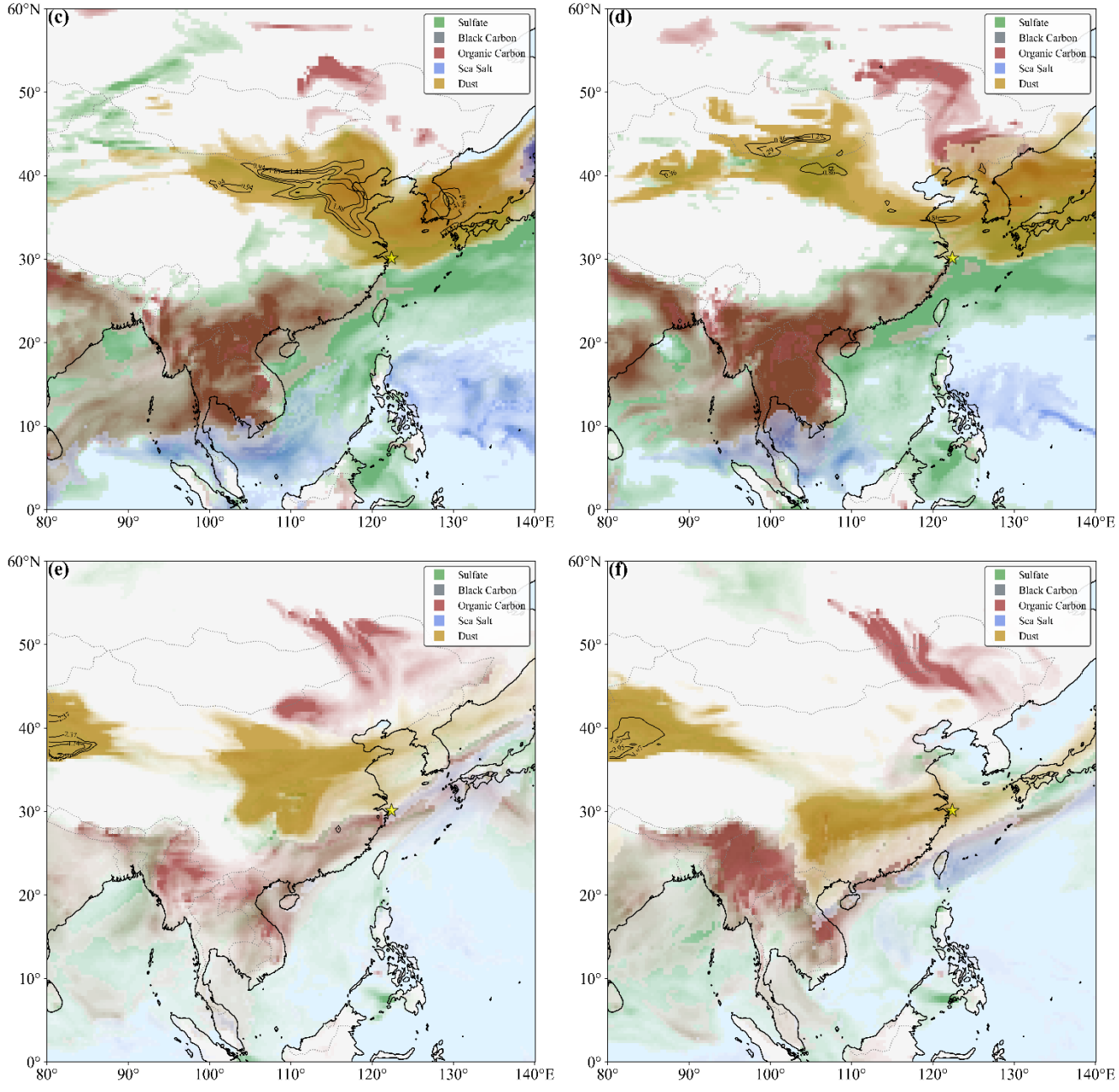

Figure 4: (a), (b), (c), (d), (e), and (f) show the distribution of different types of aerosols at 08:00 LST on March 24 (Stage 1: Pre-dust phase), 15:00 LST on March 24 (Stage 2: Dust phase), 00:00 LST on March 25, 15:00 LST on March 25 (Stage 3: Pre-formation phase of advection sea fog), 18:00 LST on March 27, and 18:00 LST on March 28 (Stage 7: Dissipation phase of mist), respectively. In the figure, green, gray, red, blue, and yellow represent sulfate, black carbon, organic carbon, sea salt, and dust aerosols, respectively.

Form Fig. 4(a), the dust had not reached the observation site at 08:00 on March 24. At the same time, the aerosols at this site were mainly sulfate aerosols. In Fig. 4(b) at 15:00 on March 24, the dust originated from Mongolia and moved

https://doi.org/10.5194/egusphere-2026-1054
Preprint. Discussion started: 4 May 2026

eastward through Inner Mongolia, Shaanxi, Shanxi, Jiangsu, and Shanghai to Qingbang Island in the East China Sea. This result is consistent with the sharp increase of aerosol PM mass concentrations at the near-surface observation site at 15:00 on March 24. This also confirms our conjecture that this increase was caused by dust passage. During Stage 2, the aerosols at this site were mainly dust particles. During Stage 2, the near-surface wind speed was relatively high and the turbulent kinetic energy was enhanced. This led to the strengthening of vertical mixing in the boundary layer. The dust in and above the boundary layer was fully mixed and settled to the near-surface. Therefore, the aerosol PM mass concentrations at the near-surface showed a significant sharp increase. From Fig. 4 (c) and (d), during Stage 3 (pre-formation phase of advection sea fog), dust always existed above the study area. The direct contribution to near-surface PM concentrations was relatively weakened. This indicates that dust aerosols were undergoing a slow settling process. Fig. 4 (d) further shows that the dust at the observation site was weakening before sea fog formation. The high-value area of dust AOD was transported to northeastern China. Fig. 4 (e) and (f) indicate that during Stage 7 (dissipation phase of mist), dust passed through the observation site again, which may accelerate its dissipation.

To further study the impact of aerosols on the formation and dissipation mechanism of this sea fog, based on the aerosol component AOD product of the H-9 satellite, the bilinear interpolation method was used. The temporal variation characteristics of AOD for sulfate, black carbon, organic carbon, sea salt, and dust aerosols at Qingbang Island in the East China Sea were calculated (Fig. 5(a)). Based on this, the average contribution rates of different types of aerosols during the entire study period were calculated (Fig. 5(b)).

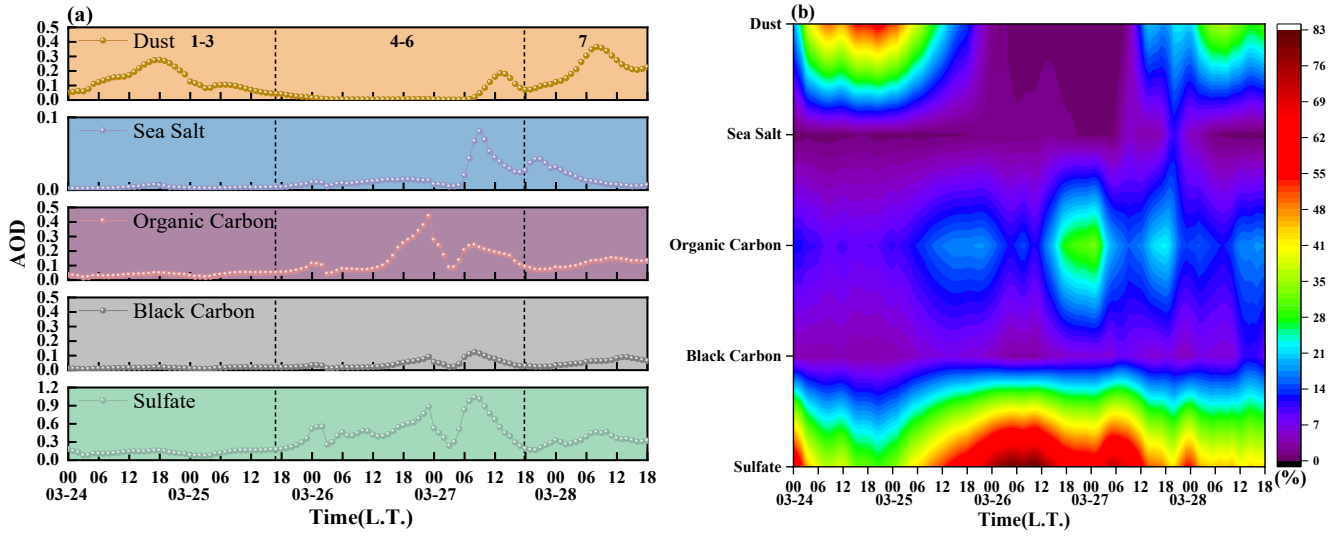

Figure 5: (a) and (b) show the temporal variation of AOD and the contribution rates of sulfate, black carbon, organic carbon, sea salt, and dust aerosols at Qingbang Island in the East China Sea, respectively.

From Fig. 5 (a) and (b), it can be seen that dust aerosol particles dominated and contributed the most during Stage 1-3(01:00 on March 25) before the outbreak of sea fog. The aerosol contributions from high to low were dust, sulfate, organic

https://doi.org/10.5194/egusphere-2026-1054
Preprint. Discussion started: 4 May 2026

carbon, black carbon, and sea salt aerosols. It is notable that the contribution of sea salt aerosols was the lowest. This indicates that the aerosols at the observation site were mainly dominated by long-distance dust transport during this stage.

During the pre-formation phase of advection sea fog (Stage 3), the dust AOD was gradually decreasing. The sulfate AOD was gradually increasing and became the dominant component. The contribution of sea salt remained at a low level. Dust and sulfate showed significant coupling characteristics. This close coupling in temporal and spatial may be related to the complex mixing and aging processes that dust experienced during long-distance transport and cross-sea transport. Previous studies have shown that in the marine atmospheric environment, Fe ions on the surface of dust can accelerate the formation of sulfate through the Fe-S coupling mechanism (Zhuang et al., 1992; Duce et al., 1980; Martin et al., 1994). This is highly consistent with the gradually increasing trend of sulfate AOD observed in our study. Previous studies have shown that dust particles can form a mixed structure of dust core and sulfate shell during the aging process. This internal mixing state can enhance the hygroscopicity of dust and effectively reduce the critical supersaturation required for its activation. This makes it easier to transform into cloud condensation nuclei (CCN) (Li et al., 2025; Tobo et al., 2010; Sullivan et al., 2009; Ma et al., 2013; Yin et al., 2007). In addition, the large accumulation of sulfate aerosols can cause a cooling effect on the atmosphere due to its negative forcing on solar radiation. Combined with the continuous moist advection, this further promotes the formation of sea fog.

During the sea fog and maintenance stages (Stage 4-6), the sulfate AOD did not decrease. Instead, it remained at a high level and contributed the most to sea fog. This is consistent with the research results of Zhao (Zhao et al., 2022). Combined with the characteristic that the contribution of sea salt aerosols always remained at a low level, the sulfate aerosols during this stage may contain secondary products from heterogeneous reactions during the aging process of dust. During the mist dissipation phase (Stage 7), the dust AOD increased significantly. This may cause cooling through the combined effect of scattering to reduce surface shortwave radiation and cold air. At the same time, it changed the stratification stability. This finally led to the evaporation of fog droplets, the increase of visibility, and the dissipation of mist. This further verifies the conjecture in Fig. 4 (e) and (f) that the dissipation of sea fog is related to the second passage of dust. In summary, dust aerosols may have played a dual role in this dust-sea fog event. During the pre-formation phase of sea fog (Stage 3) and the mist dissipation phase (Stage 7), the temperatures both showed a decreasing trend. In Stage 3, when the RH increased, dust may have transformed into more hygroscopic mixed-state aerosols through the aging process, promoting the formation of sea fog. In Stage 7, when the RH decreased, dust inhibited the maintenance of mist.

To further understand the microphysical and optical properties of aerosols during this event, the following analysis was conducted. Based on the mass concentrations of near-surface pollutants PM_1, $PM_{2.5}$, and PM_{10} during the observation period, the proportions of aerosol particle size distributions in the ranges of 0-1, 1-2.5, and 2.5-10 μm were calculated. The results of aerosol mass extinction efficiency (MEE) were also calculated (Fig. 6).

https://doi.org/10.5194/egusphere-2026-1054
Preprint. Discussion started: 4 May 2026

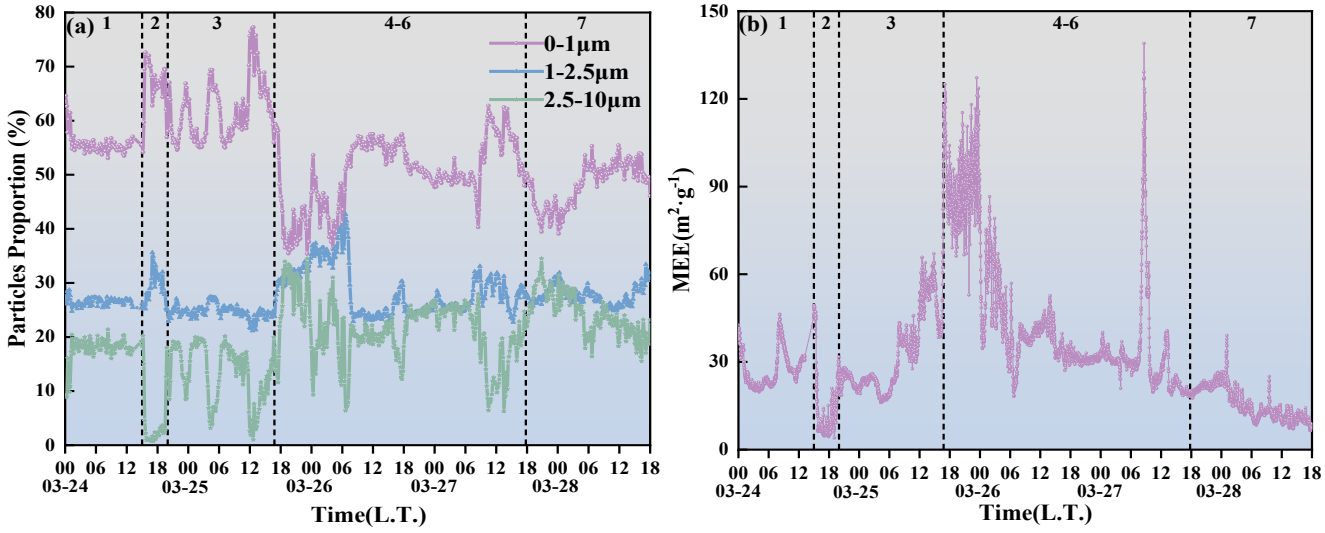

Figure 6: (a) and (b) show the mass concentration proportions of aerosol particle size distributions in the ranges of 0-1, 1-2.5, and 2.5-10 μm, and the temporal variation of aerosol mass extinction efficiency, respectively.

From Fig. 6(a), during the dust period (Stage 2, 15:00-20:00 on March 24), the proportion of aerosols with particle sizes of 0-1 and 1-2.5 μm significantly increased, while the proportion of aerosols with particle sizes of 2.5-10 μm decreased significantly (by 19%). This phenomenon is related to the typical characteristics of long-distance dust transport. During the transport process, fine particles (0-1 μm and 1-2.5 μm) can remain suspended over long distances due to their lower mass and slower settling rate. This also indicates that during the long-distance transport of dust passing through the observation site, dust aerosols were mainly fine particles. The particle size was mainly concentrated in the 0-2.5 μm. In addition, the dust transport passed through regions with strong pollution emissions. Dust particles may have mixed and interacted with regional pollutants, undergoing a certain degree of chemical aging.

In the early period of Stage 3, aerosols were mainly submicron particles (0-1 μm). However, after the RH increased to 90% at 12:40 on March 25, a significant modal shift occurred in the aerosol particle size distribution. During Stage 3 (12:40-16:47 on March 25) and the early period of Stage 4 (16:47-19:30 on March 25), the proportion of particles with sizes of 0-1 μm decreased by 18% and 24%, respectively, while the proportion of particles with sizes of 1-2.5 μm increased by 5% and 4%, respectively, and the proportion of particles with sizes of 2.5-10 μm increased by 13% and 20%, respectively. Combined with the result in Fig. 5 that the contribution of sea salt remained at a low level, this modal shift was mainly attributed to the strong hygroscopicity of aged dust and its mixed-state aerosols with sulfate. At the same time, this also indicates that before and in the early period of sea fog formation, a large number of submicron particles acted as CCN and underwent explosive hygroscopic growth in the near-saturated environment, then activated into fog droplets. In the middle and late period of Stage 4, the proportions of particles with sizes of 0-1 μm and 1-2.5 μm showed oscillating increases, while the proportion of particles with sizes of 2.5-10 μm showed an overall oscillating decrease. This phenomenon was attributed to the gravitational settling and wet removal effect of large fog droplets. During Stage 5, the proportions of all particle sizes showed oscillating

https://doi.org/10.5194/egusphere-2026-1054
Preprint. Discussion started: 4 May 2026

variation trends, and the PM mass concentrations showed an overall oscillating decrease. This indicates the dynamic competition between external transport and wet removal by fog droplets, ultimately resulting in the wet removal effect of fog on aerosols.

In the early period of Stage 6, the proportions of particles with sizes of 0-1, 1-2.5, and 2.5-10 μm basically showed a balanced oscillating trend. However, a short-term sea fog disturbance event occurred during 08:08-09:05 on March 27. During the early period of the sea fog disturbance (07:10-08:30 on March 27) and during the disturbance (08:30-09:05 on March 27), the variation characteristics of aerosol particle size were highly consistent with the variation trends in Stage 3 (12:40-16:47 on March 25) and the early period of Stage 4 (16:47-19:30 on March 25). In the late period of Stage 6 and the early period of Stage 7, the proportions of aerosol particles with sizes of 0-1 and 1-2.5 μm decreased by 23% and 4%, respectively, while the proportion of aerosol particles with sizes of 2.5-10 μm increased by 27%. Interestingly, compared with the particle size variation characteristics at before and in the early period of sea fog formation, only the trend of the proportion of aerosol particles with sizes of 1-2.5 μm was opposite. At the same time, the RH was continuously decreasing. his indicates that there are non-hygroscopic physical processes at play at this time, such as external transport. This corresponds to the satellite monitoring result in Fig. 3(a) that dust invaded the observation site again. At the same time, it changed the atmospheric radiation-thermal conditions and enhanced the boundary layer mixing, further promoting the complete dissipation of mist.

In Fig. 6(b), during the dust passage (early period of Stage 2), the MEE decreased by 87% compared with the baseline before dust arrival. This indicates that the extinction efficiency per unit mass of dust aerosols was significantly lower under low RH conditions. As the RH increased (late period of Stage 2 to Stage 3), the MEE showed an oscillating increase. In the early period of sea fog formation (early period of Stage 4), the MEE increased by 2.3 times, reaching 125 m^2g^{-1}. During the sea fog period (Stage 4), the MEE mostly remained between 70-120 m^2g^{-1}. This indicates the dominant contribution of fog droplets to extinction, keeping the visibility at low values. Subsequently, during the alternating evolution phase of advection sea fog and mist (Stage 5), the MEE showed an obvious oscillating decrease. This was related to the gravitational collision and wet removal processes of fog droplets. During the short-term sea fog disturbance in Stage 6, the MEE showed a peak value as high as 139 m^2g^{-1} again, increasing by 4.3 times. This further verifies that fog droplets have a strong extinction effect during the sea fog process. After entering the dissipation period, the RH continued to decrease. With the second invasion of dust, fog droplets disappeared and aerosols turned to dry state, and the MEE decreased rapidly.

The modal shift of particle size and the enhancement of MEE confirmed the hygroscopic growth characteristics of dust aerosols after aging from the microphysical and optical perspectives. To understand how aerosol mass concentration and RH affect the macroscopic visibility evolution of this event, the meteorological station observation data (PM mass concentration, Vis, RH) during the entire process were used. This aimed to explore the relationship of visibility to PM mass concentration and its sensitivity to RH (Fig. 7).

https://doi.org/10.5194/egusphere-2026-1054
Preprint. Discussion started: 4 May 2026

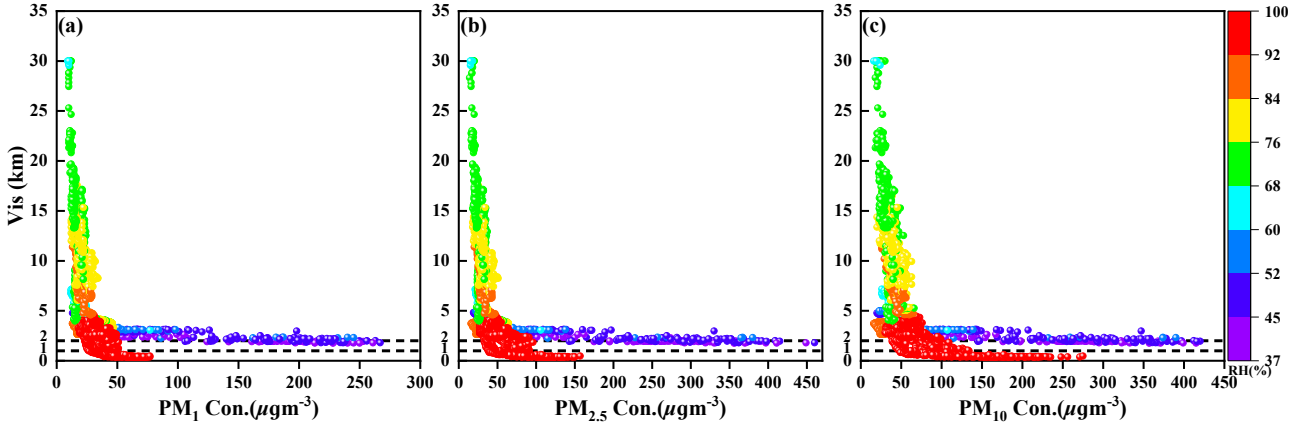

Figure 7: The relationship between visibility and PM mass concentration modulated by RH during the dust-sea fog event from March 24-28, 2025.

The results of Fig. 7 (a, b, c) all show that there was a typical exponential decay relationship between visibility and aerosol mass concentration. However, the decay rate was strictly controlled by the RH. During the low RH phase of dust passage (as shown in the blue-purple colour results at around 2-5 km in the figure), the sensitivity of visibility to PM concentration was relatively low. The exponential decay result showed a high exponential decay rate in the sea fog under high RH conditions. When the visibility was in the range of 0-1 km, the mass concentrations of PM_1, $PM_{2.5}$, and PM_{10} were in the ranges of 26-77, 38-157, and 47-275 μgm^{-3}, respectively. The low critical thresholds for sea fog occurrence were 26, 38, and 47 μgm^{-3}, respectively. This significant result indicates that only a low aerosol mass concentration is needed to trigger sea fog. This phenomenon is highly consistent with the previous result that aged dust and its mixed-state aerosols with sulfate can enhance their hygroscopicity. At the same time, this indicates that aged dust and its mixed-state aerosols with sulfate can act as efficient CCN. They have a strong exponential decay effect on visibility under high RH conditions.

3.3 Radiation Characteristics and Thermal Stratification Structure of the Boundary Layer

Aerosols regulate the surface energy budget through radiative effects (Huang et al., 2014; Bellouin et al., 2020; Liu et al., 2021). However, the influence of surface radiation processes on the thermodynamic structure of the boundary layer (Deaconu et al., 2019; Graaf et al., 2020) directly affects the formation, maintenance, and dissipation of sea fog. The temporal evolution results of radiation parameters and the evolution results of boundary layer temperature with time and space during the observation period (Fig. 8 and Fig. 9) were used to analyse how radiation affects the stable structure of the boundary layer and the evolution characteristics of the sea fog life cycle.

https://doi.org/10.5194/egusphere-2026-1054
Preprint. Discussion started: 4 May 2026

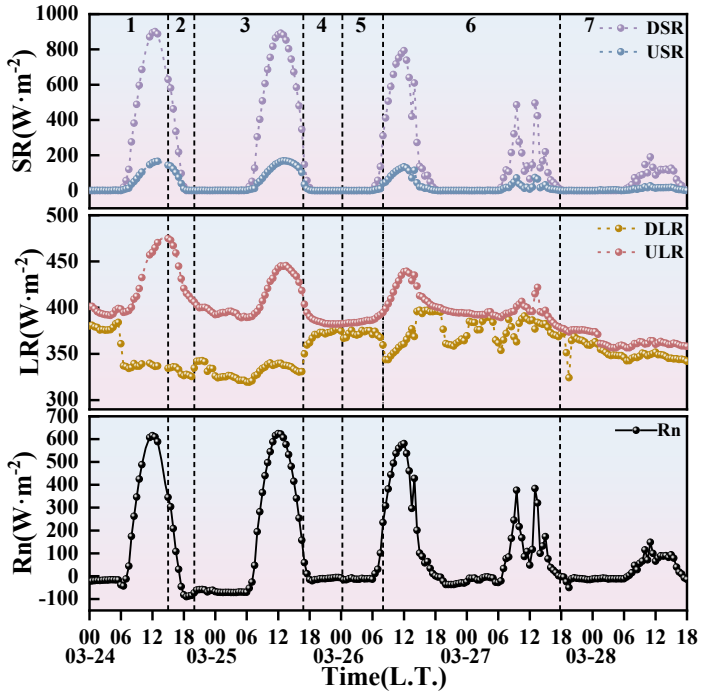

Figure 8: Evolution of near-surface radiation parameters with time during the event from March 24-28, 2025 (SR: shortwave radiation, DSR: downward shortwave radiation, USR: upward shortwave radiation, LR: longwave radiation, DLR: downward longwave radiation, ULR: upward longwave radiation, Rn: net radiation).

Fig. 8 shows that from Stage 1 to Stage 2, the radiation field changed from typical clear-sky diurnal variation characteristics to attenuation characteristics dominated by aerosol radiative forcing. During Stage 2, dust aerosols increased the attenuation rate of DSR through their scattering and absorption effects. DLR did not weaken with the decrease of solar elevation angle, in the early period of dust passage, but remained at about 335 W·m^{-2}. This confirms that the dust layer compensated energy to the surface through thermal radiation after absorbing shortwave radiation. However, with sunset and the gravitational settling of dust, ULR showed an attenuation trend. Rn turned negative early at 17:30 on March 24, indicating that the surface energy budget reversed from surplus to deficit. In Stage 3, with the increase of sulfate aerosol concentration and its mixing with dust, aerosols showed strong scattering characteristics. Observations showed that DSR decreased by 744 W·m^{-2} from 12:30 to 17:00 on March 25. The decrease rate was 8% higher than that under clear-sky background (the same period in Stage 1-2). This further reflects that the radiative properties of different types of aerosols can change the surface-atmosphere radiation balance and heating or cooling rate, and then change the PBL structure. The strong scattering effect of sulfate aerosols combined with water vapor accumulation provided the necessary thermodynamic preconditions for the subsequent condensation and outbreak of sea fog in the near-surface layer.

The value of DSR and USR rapidly decreased to zero and remained after dust settling and sea fog formation. This indicates that the surface lost the direct heating source of sun. However, DLR increased obviously from 330 W·m^{-2} to 374 W·m^{-2}. This was attributed to the significant enhancement of atmospheric reverse radiation by the dense fog layer. ULR

https://doi.org/10.5194/egusphere-2026-1054
Preprint. Discussion started: 4 May 2026

showed a weakening trend and then remained at 382 W·m^{-2}, due to the continuous surface cooling and longwave radiative cooling at the fog top. At the same time, Rn rapidly changed from positive to negative and remained negative. This continuous net radiation deficit would enhance the boundary layer stability, which is favourable for the maintenance and development of fog. DLR fluctuated slightly around 371 W·m^{-2} during Stage 5. This indicates that the fog layer thickness or the interior of the fog changed. This is also the result of the alternating evolution of advection sea fog and mist. Rn changed from negative to positive after sunrise on March 26 (234.8 W m^{-2} at 08:00 on March 26). This indicates that the surface regained net energy input, driving fog droplet evaporation and promoting the system to evolve toward mist. All radiation parameters showed high-frequency oscillating non-steady characteristics during the mist period. Especially, DLR was the most sensitive, which directly reflects the fluctuation of fog top height, the uneven liquid water content, and the rapid evolution of fog layer thickness during the mist process. Finally, cold air carrying dust invaded the observation site with a daytime cumulative precipitation of 3.8 mm. The thermal balance was destroyed, blocking the microphysical conditions for fog droplet maintenance, and the mist completely dissipated.

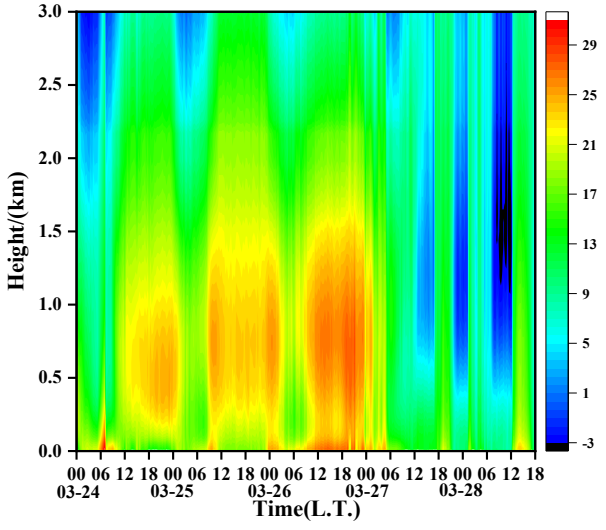

Figure 9: Boundary layer temperature with time and height from March 24-28, 2025.

Fig. 9 shows that an inversion structure began to form in the near-surface layer at 10:00 on March 24, mainly concentrated at 0.4-1 km. Its occurrence and development were related to the continuous increase of dust AOD observed by satellite on March 24 (Fig. 5(a)). With dust passage and continuous settling, the inversion intensity in the near-surface layer continued to increase, with the maximum inversion intensity reaching 9°C. At the same time, the thickness of the inversion layer also expanded significantly. This strong inversion layer was favourable for the accumulation of dust aerosols of sea surface and provided initial thermal conditions for the stabilization of the lower atmosphere. From 09:00 to 16:47 on March 25, with the establishment of sea breeze carrying warm and moist airflow over the cold sea surface, a continuously stable and deeper inversion layer formed in the boundary layer. This accelerated the continuous accumulation and physicochemical reactions of aerosols, providing sufficient CCN and ideal thermodynamic conditions for the outbreak of sea fog. During

https://doi.org/10.5194/egusphere-2026-1054
Preprint. Discussion started: 4 May 2026

Stage 4 (advection sea fog period), warm and moist advection and the stable and deep inversion layer continued to exist. This is highly consistent with the continuous negative net radiation results at the near-surface. The combined effect of surface cooling and longwave radiative cooling at the fog top continuously strengthened the stability of the boundary layer, which was favourable for the formation and maintenance of sea fog. In Stage 5, there were signs of warming at the bottom of the inversion layer and the overall inversion intensity weakened, marking the beginning of the initial decay period of the system. At 06:00 on the 26th, the combined effect of the increase of DSR and turbulent mixing began to erode the cold air near-surface, causing some fog droplets to evaporate. This resulted in the oscillating characteristics of alternating between sea fog and mist. The thermal structure of the boundary layer became complex during the mist maintenance stage, with multi-layer thermal structures and instantaneous disturbances. This is consistent with the high-frequency fluctuations of radiation parameters SR, LR, and Rn. Finally, the original inversion structure had completely disintegrated, and a top-down mixing cooling process occurred. This may be related to large-scale synoptic systems. The intrusion of dry and cold air broke the warm, moist, and stable thermal conditions required for mist maintenance.

3.4 Analysis of Turbulence Characteristics

The life cycle of sea fog depends not only on aerosol and radiation effects, but is also finely regulated by near-surface turbulence disturbances. Turbulence is a key dynamic factor determining the formation, maintenance, and dissipation rate of fog by regulating the mixing intensity and turbulent transport. Therefore, the near-surface high-frequency observation data collected by CSAT3 were used in this study. The results of turbulence intensity (I_u, I_v, I_w), horizontal wind speed (U), friction velocity (u_*), turbulent kinetic energy (TKE), and stability parameter (ζ) with time were calculated (Fig. 10).

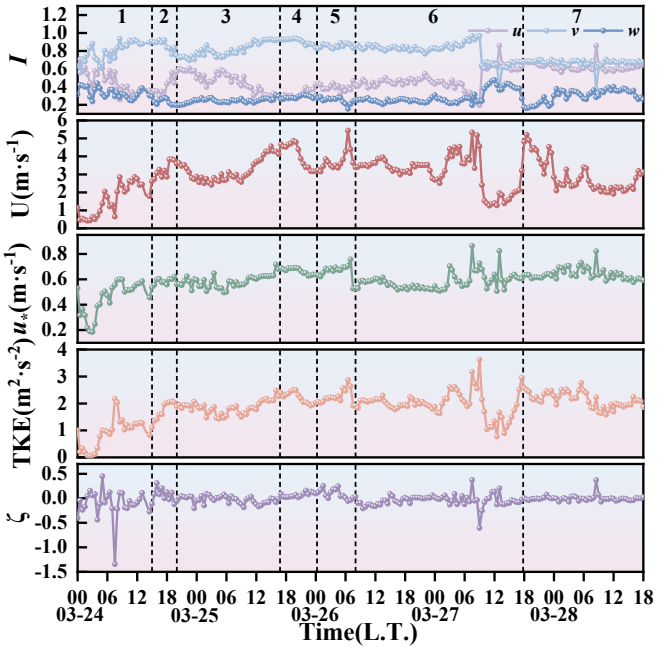

https://doi.org/10.5194/egusphere-2026-1054
Preprint. Discussion started: 4 May 2026

Figure 10: Evolution of near-surface turbulence parameters with time during the dust-sea fog event from March 24-28, 2025.

Fig. 10 shows that TKE exhibited significant diurnal variation characteristics before dust passage (Stage 1), with a peak at 07:30 on March 24. This was mainly controlled by thermal buoyancy driven by shortwave radiation. However, with the passage of dust aerosols (Stage 2), the turbulence structure showed characteristics of dynamic enhancement and thermal stability. Although U, TKE, and u_* all showed an overall increasing trend, providing a strong mechanical shear source, ζ rapidly turned positive (ζ > 0 for 60% of the time) due to the forcing of radiative cooling effect of the dust layer. This is consistent with the boundary layer inversion in physical mechanism. With the establishment of sea breeze (Stage 3), U (U increased to 4.67 $m \cdot s^{-1}$ at the end of Stage 3), TKE, and u_* first decreased and then increased. The stability parameter ζ was close to neutral. After the establishment of the sea breeze stability, the enhancement of turbulence promoted the rapid formation of sea fog.

During Stage 4, the boundary layer showed strongly stable characteristics (ζ was all positive). The turbulence intensity (I_v, I_w) was limited, which was favourable for the formation and development of sea fog. This was related to the radiative cooling at the fog top and the long-term maintenance of boundary layer inversion (Fig. 8, 9). This result is consistent with the strengthening of stratification stability by negative Rn. Before 20:00 on March 25, TKE and U synchronously first decreased and then increased. At the same time, u_* remained at a high level, indicating that mechanical turbulence was relatively high. In the later period, TKE weakened accordingly with the decrease of U. Overall, this turbulence structure maintained the material exchange in the near-surface layer (supporting the hygroscopic growth of aerosols, the continuous interaction with fog droplets, and extinction with fog droplets). This also explains the observation results of the coexistence of continuously low visibility and multi-peak fluctuations of aerosol mass concentration PM during this period.

In the morning of March 26 (Stage 5), although the stratification was still mainly stable, the resumed an upward trend of DSR (Rn turned positive) and the enhancement of local shear triggered intense instantaneous turbulence fluctuations (U instantaneously reached 5.43 m/s at 06:30, TKE reached 2.874 m^2/s^2, and u_* reached 0.756 $m \cdot s^{-1}$ at 07:00 on March 26). This fluctuation broke the previous quasi-steady equilibrium, accelerated the wet removal and collision of fog droplets, and promoted the transformation from dense fog to mist. Subsequently, the system entered a strong non-steady oscillation period (Stage 6). Especially during 06:30-09:00 on March 27, the sharp rise and turbulence parameters (U, u_*, TKE, ζ) corresponded to a dense fog disturbance. Then dry and cold northwest wind intruded. The turbulence intensity showed dramatic changes (I_v dropped sharply, I_u and I_w rose sharply). This indicates that the turbulence components underwent rapid reorganization. The vertical mixing efficiency improved, and the phase equilibrium was disrupted, while accelerating the evaporation and entrainment of fog droplets. After 09:00 on the 27th, U and TKE showed a sharp drop followed by a rapid increase trend before the end of Stage 6. This led the system to enter irreversible dissipation. The observation of the meteorological station showed that the ground was still in mist during this period. This indicates that the macroscopic dissipation of fog lagged behind the pulsation mutation of turbulence, showing a significant characteristic of turbulence acting first and fog responding later. Finally (Stage 7), I_u and I_v remained at relatively high values. At the same time, I_w gradually increased, indicating that horizontal and vertical turbulent mixing and entrainment in the boundary layer were

https://doi.org/10.5194/egusphere-2026-1054
Preprint. Discussion started: 4 May 2026

relatively active at this time, with strong turbulent exchange capacity. Dust again invaded, and the mechanical turbulent mixing dominated by dry and cold northwest wind further enhanced the momentum exchange in the lower atmosphere. At this time, the RH decreased significantly, the water vapor competition effect intensified, the phase equilibrium between aerosols and fog droplets was disrupted, causing the fog droplets to rapidly evaporate, and the system completely dissipated.

To further clarify the threshold ranges of turbulence parameters required during sea fog, the relationships between PM_{10} mass concentration (representing total aerosol mass concentration) and key turbulence parameters (I_u, I_v, I_w, TKE, u_*, U) during Stage 4-6 were analysed (coloured by Vis) (Fig. 11).

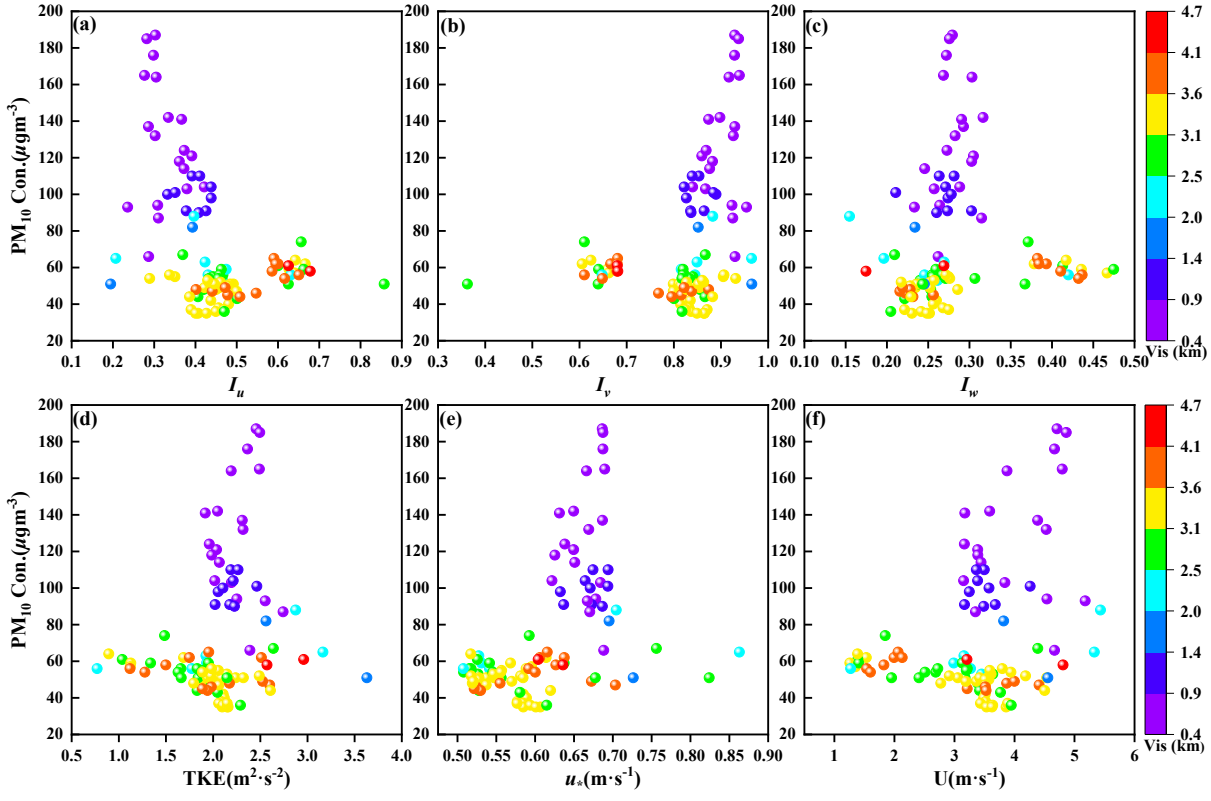

Figure 11: Relationships between PM_{10} mass concentration and key turbulence parameters during the fog period (Stage 4-6, RH > 95%) (coloured by Vis).

A clear result in Fig. 11 (a-f) all consistently show, when PM_{10} mass concentration exceeded 80 μgm^{-3}, Vis was mostly below 1 km. Based on this characteristic threshold, the threshold ranges of turbulence parameters for maintaining sea fog below 1 km were also relatively obvious. The thresholds of U and TKE were concentrated in the ranges of 3.1-5.1 ms^{-1} and 1.91-2.74 m^2s^{-2}, respectively. It is notable that the u_* was limited to a significantly narrow range of 0.62-0.69 ms^{-1}. This indicates that the sea fog has extremely high sensitivity to u_*. The thresholds of I_u, I_v, and I_w were concentrated in 0.2-0.4, 0.8-0.95, and 0.21-0.31, respectively. This moderate turbulence threshold range established a quasi-steady dynamic equilibrium. This turbulence intensity was sufficient to maintain the co-suspension of high-concentration aerosols and fog

https://doi.org/10.5194/egusphere-2026-1054
Preprint. Discussion started: 4 May 2026

droplets under near-saturated conditions. At the same time, it was effectively limited below the critical value, thus avoiding the dissipation of sea fog caused by stronger entrainment or mechanical turbulence at higher intensity.

3.5 Synoptic and Marine meteorological conditions at the sea-vapor interface

The microphysical and radiative properties of aerosols and the dynamic characteristics of local turbulence had synergistic effects in regulating the life cycle of sea fog during this event. However, the realization of this regulatory effect depends on specific circulation background and air-sea conditions. Aerosols, radiation, and turbulence provide potential microphysical regulatory factors. The large-scale and local meteorological conditions of the air-sea system are the key background determining whether sea fog can form, maintain, and dissipate. To systematically study the external driving mechanisms behind the evolution of sea fog and macroscopic characteristics, the comprehensive influence mechanism of multi-scale circulation and air-sea conditions on the evolution process of sea fog was studied through the elements of 850 hPa geopotential height, sea level pressure and RH, near-surface air temperature and wind field, and air-sea temperature difference (Fig. 12).

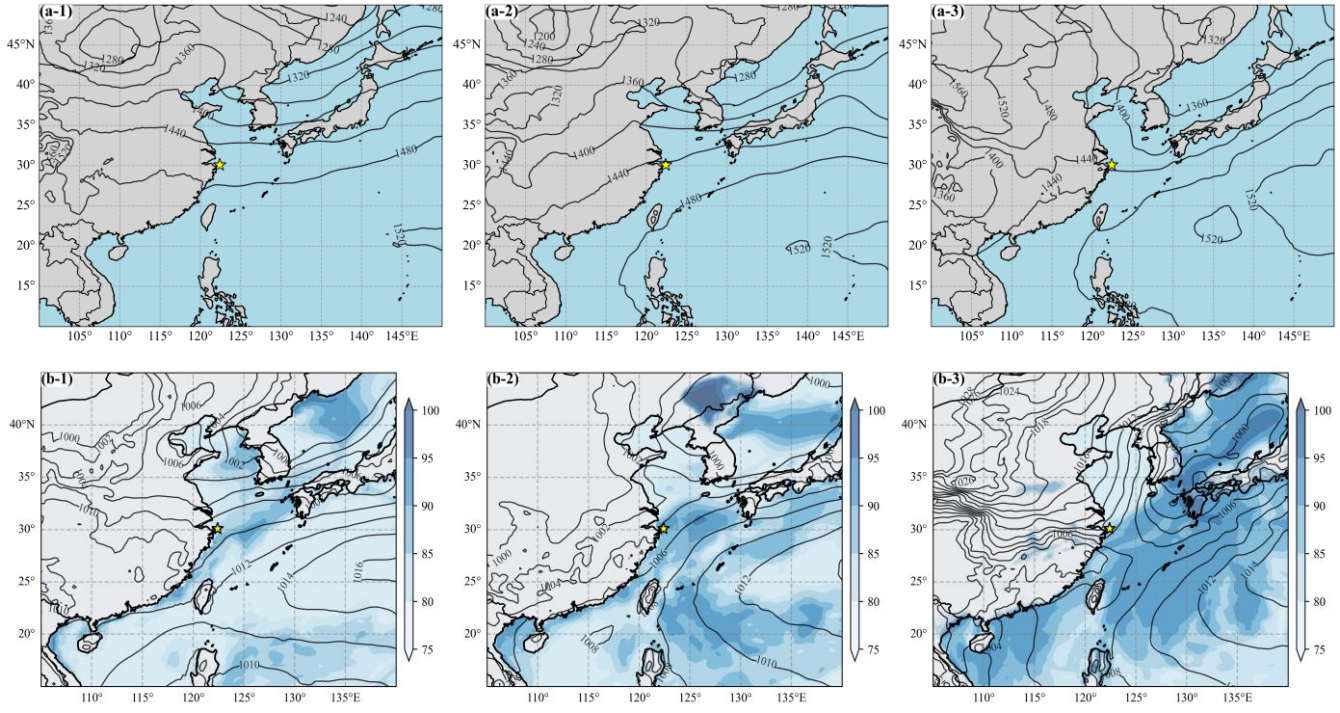

https://doi.org/10.5194/egusphere-2026-1054
Preprint. Discussion started: 4 May 2026

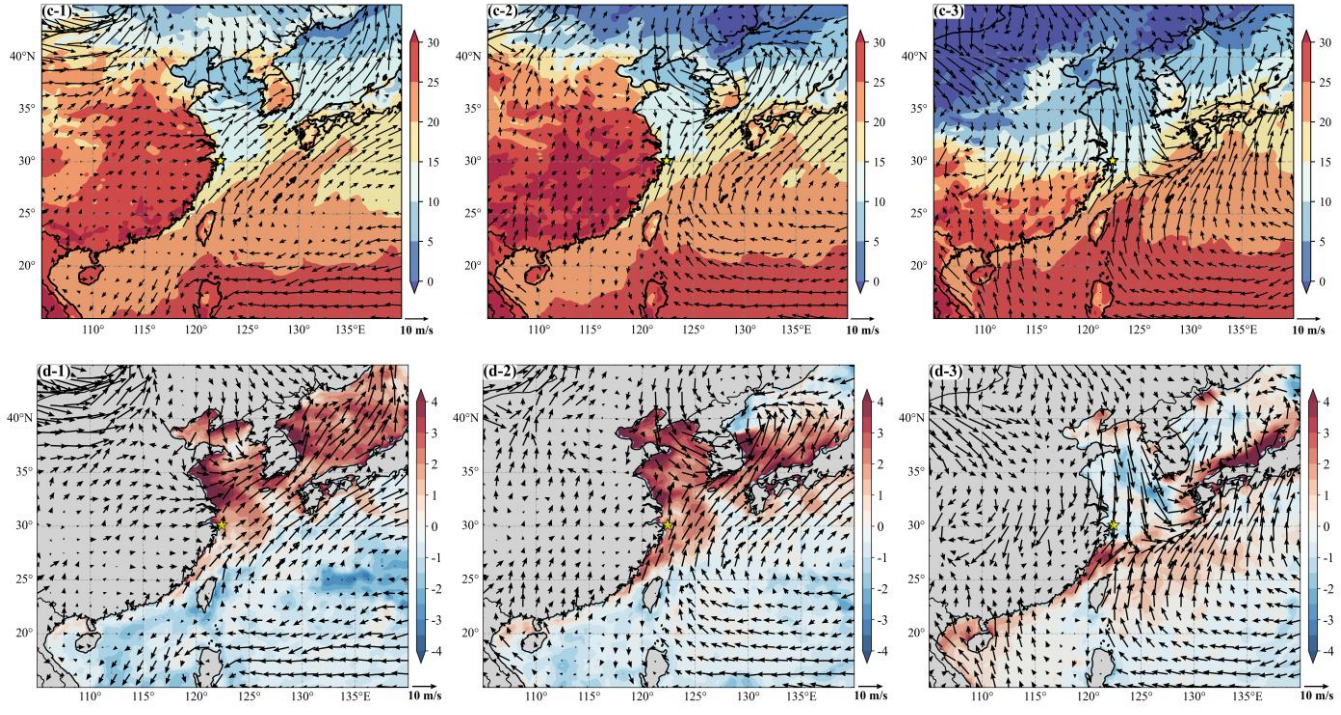

Figure 12: (a-k), (b-k), (c-k), and (d-k) (k=1, 2, 3) show the 850 hPa geopotential height (contour, gpm), sea level pressure (contour, hPa) and RH (shaded, %), 2-m air temperature (shaded, ℃) and horizontal wind (m/s), and air-sea temperature difference (shaded, ℃) and horizontal wind (m/s) at 3 different time, respectively. k=1 is Stage 2 (dust period) at 15:00 on March 24, k=2 is Stage 4 (advection sea fog period) at 17:00 on March 25, and k=3 is Stage 7 (mist dissipation period) at 18:00 on March 27.

During the dust period (Stage 2), Fig. 12 (a-1) shows that the northwest region of China was controlled by the Mongolian cyclone, with a central geopotential height of 1280 gpm. A strong westerly low-level jet formed in the south of this cyclone. This westerly jet served as an efficient transport channel, transporting dust particles from Mongolia and Inner Mongolia to the observation site at Qingbang Island in the East China Sea of China. Fig. 12 (b-1, c-1) show that a cold air mass moved southward along the Bohai Sea, forming an obvious cold tongue structure. In addition, the observation site was at the convergence of the westerly wind from the dust transport channel and the southerly wind carrying warm and moist airflow from the southeast. This showed the characteristic of dust passage accompanied by moistening. At this time, the observation site was not yet controlled by the core area of cold air, but located at the junction of cold and warm air. The air-sea temperature difference was 1.5°C (Fig. 12 (d-1)). The Mongolian cyclone provided dynamics and channel for dust transport. The moistening effect at the convergence of cold and warm air created initial conditions for the physicochemical reactions of aerosols. The positive air-sea temperature difference laid the thermal foundation for sea fog formation.

During the advection sea fog period (Stage 4), Fig. 12 (a-2) shows that the Mongolian cyclone in Stage 2 had moved eastward over the Bohai Sea to the coastal area of the Korean Peninsula, and established and developed a low-pressure trough in this area. At the same time, a new cyclone system appeared in the northwest of Mongolia, with more intensity and

https://doi.org/10.5194/egusphere-2026-1054
Preprint. Discussion started: 4 May 2026

a central geopotential height of 1200 gpm. Under the guidance of the airflow from this new cyclone, dust was transported to the Yellow Sea and the northern East China Sea. However, the low-pressure trough over the Korean Peninsula continued to guide the dust to move eastward. This is highly consistent with the satellite-observed spatial distribution of dust in Fig. 4 (c) and (d). Fig. 12 (b-2, c-2) show that the near-surface southerly wind speed increased significantly, providing sufficient water vapor to the observation site. The RH was close to saturation and the air temperature increased. In Fig. 12 (d-2), the air-sea temperature difference was 1.8°C. Warm and moist air flowed over the cold sea surface, providing favourable conditions for the formation of typical advection cooling fog. This is consistent with the research results of Yang et al. (Yang et al., 2024). It is notable that the satellite observation results in Fig. 5 (a) show that dust existed throughout Stage 2 to the early period of Stage 4. Under high RH conditions, the mixed sulfate formed after the aging of dust underwent rapid hygroscopic growth. This greatly promoted the condensation and collision processes of fog droplets. Therefore, under the synergistic effect of favourable dynamic background (southerly wind transporting sufficient water vapor), thermal conditions (0-2°C air-sea temperature difference), and sufficient CCN, typical sea fog was able to outbreak and maintain.

During dissipation period of mist (Stage 7), Fig. 12 (a-3) shows that under the supplementation and penetration of cold air carried by the eastward movement of the new Mongolian cyclone system in Stage 4, the low-pressure trough along the coast of the Korean Peninsula was further strengthened and extended southward. The observation site was in the pre-trough area. The circulation adjustment strengthened the northerly airflow ahead of the trough, carrying dry and cold air southward along a northerly path. The surface synoptic condition showed cold front passage. Fig. 12 (b-3, c-3) show that the northerly wind speed reached 8-10 m/s. This strong dry and cold air destroyed the warm and moist environment for maintaining mist. The RH dropped sharply to 75% and the air temperature decreased significantly. In Fig. 12 (c-3), the air-sea temperature difference turned to negative (-0.15°C). This broke the thermal equilibrium required for sea fog and inhibited the maintenance of mist. At the same time, the Himawari satellite data results in Fig. 4 (e, f) show that this northerly wind process carried a new round of dust, passing through the northwest region of China, and transported it to the observation site. A large amount of dust competed for water vapor under low RH conditions and inhibited condensation. At the same time, it enhanced the evaporation of fog droplets and entrainment, accelerating the dissipation of mist.

4 Summary and conclusions

Based on the H-9 satellite remote sensing data, the high-resolution ground-based observation platform data at Qingbang Island in the East China Sea, and ERA5 data, a detailed full life cycle study on a dust-advection sea fog event from March 24-28, 2025 was study. Through comprehensive analysis of aerosol microphysical properties, radiation and boundary layer thermodynamic structure, turbulence dynamic characteristics, and the evolution of synoptic situation and air-sea conditions, the key parameters during this process were quantified. The comprehensive mechanism of typical dust-advection sea fog event was systematically studied (Fig. 13). The main conclusions are as follows:

https://doi.org/10.5194/egusphere-2026-1054
Preprint. Discussion started: 4 May 2026

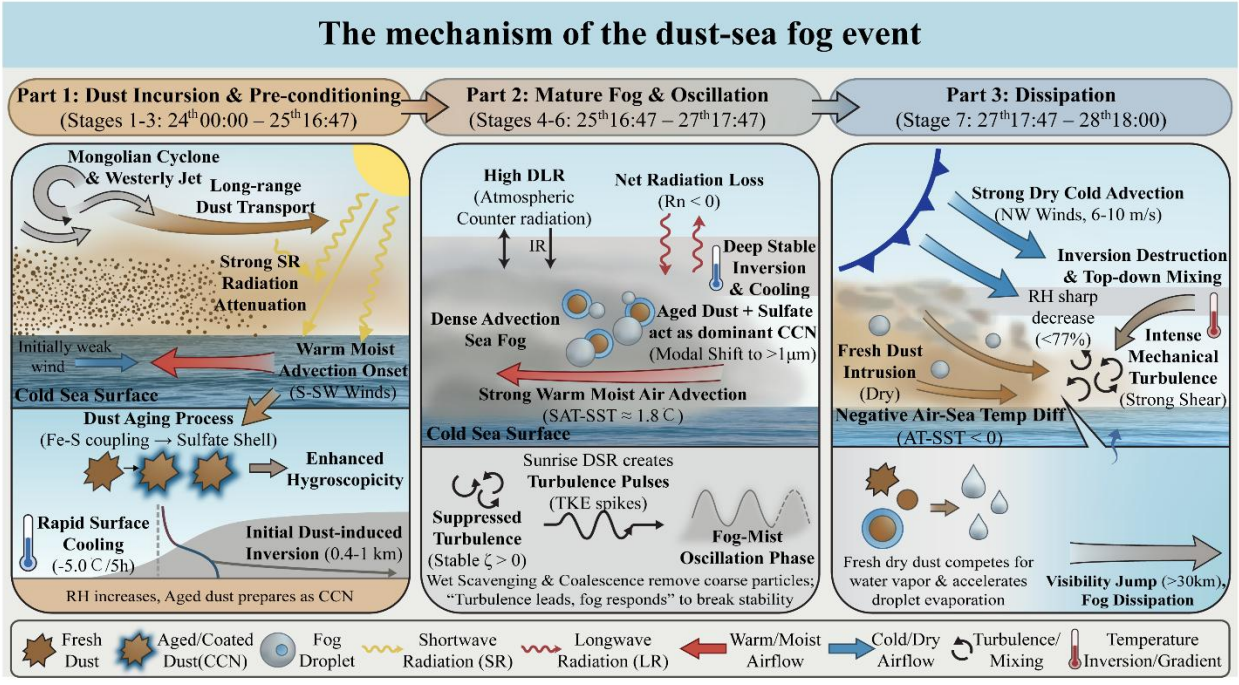

Figure 13: Mechanism of the dust-sea fog event.

This event indicates that long-distance transported dust aerosols have a promoting effect on sea fog formation under high RH conditions. Dust aerosols originating from Mongolia passed through the observation site under the guidance of the westerly jet, causing the near-surface PM_{10} mass concentration to explosively increase to 469 μgm^{-3}. Different from the traditional view in sea fog research that sea salt aerosols act as CCN, this study found that during the Stage 3 to early Stage 4, dust and sulfate aerosols showed high coupling in time and space (sulfate AOD showed an increasing trend). The dust particles underwent complex aging processes (Fe-S coupling mechanism promoted sulfate formation, and mixed sulfate formed after dust aging). During Stage 3 (12:40-16:47 on March 25) and early Stage 4 (16:47-19:30 on March 25), the aerosol particle size distribution showed obvious modal shift. The proportion of 0-1 μm particles decreased by 18% and 24%, respectively, while the proportion of 1-2.5 μm particles increased by 5% and 4%, respectively, and the proportion of 2.5-10 μm particles increased by 13% and 20%, respectively. This significantly enhanced the hygroscopicity of dust. When the RH rose to 90%, sulfate aerosols could replace sea salt as the dominant CCN and underwent explosive hygroscopic growth. This also confirms that the cross-modal transformation of aerosols to fog droplets is the core microphysical cause of the sharp drop of Vis to below 1.0 km.

Dust aerosols significantly changed the thermodynamic structure of the boundary layer through direct radiative effects, constructing an ideal background for the formation of advection sea fog. Dust aerosols reduced DSR through scattering and absorption effects and increased the attenuation rate of DSR. This caused the near-surface temperature to drop sharply by 5.0°C within 5 hours, forming an inversion. The inversion was mainly concentrated at 0.4-1 km, with the maximum

https://doi.org/10.5194/egusphere-2026-1054
Preprint. Discussion started: 4 May 2026

inversion intensity reaching 9°C. Previous studies on advection sea fog mostly emphasized the advective cooling effect. However, this study found that the radiative cooling of dust formed an inversion before sea fog formation, enhancing the stability of the boundary layer in advance. This early inversion (Stage 2) superimposed with the subsequently established warm and moist advection (the SAT-SST was 1.8°C in Stage 3), providing favourable thermodynamic conditions and stratification stability for the occurrence of sea fog. During the advection sea fog period (Stage 4), the dense fog layer caused the net radiation (Rn) to remain continuously negative. This kept the MEE at a high level of 70-120 m^2/g, establishing the long-term maintenance of the sea fog system. The study found that DLR was the most sensitive to the state changes of sea fog (fluctuations of fog top height, uneven liquid water content, and fog layer thickness).

The turbulence characteristic study found that the boundary layer showed strongly stable characteristics ($\zeta > 0$) during the advection sea fog period (Stage 4). The turbulence intensity (I_v, I_w) was limited, which was favourable for the formation and development of sea fog. However, during the alternating period of advection sea fog and mist (Stage 5), the recovery of shortwave radiation after sunrise triggered turbulence fluctuations. This broke the stable stratification and accelerated the gravitational collision and wet removal of fog droplets ($PM_{10} > PM_{2.5} > PM_1$). It is notable that dust played different roles in different life stages of sea fog. Aged dust acted as CCN to promote sea fog formation during late Stage 3 to early Stage 4 (high RH). During the dissipation stage of mist (late Stage 6), the dynamic evolution pattern of turbulence acting first and fog responding later was found. During the dissipation period of mist (Stage 7, low RH), with the intrusion of dry and cold northwest wind (8-10 m/s) carrying dry dust, the air-sea thermodynamic equilibrium was destroyed (SAT-SST turned to -0.15°C). Intense mechanical turbulent mixing and water vapor competition effect accelerated the evaporation of fog droplets and entrainment, resulting in an increase in visibility to 30 km.

This event is a typical coupled case of dust-advection sea fog with synergistic effects of multiple influencing factors. The large-scale circulation background provided sufficient water vapor, dust transport channels, and suitable air-sea conditions. Aerosols and radiation can change the microphysical properties of sea fog and the thermodynamic structure of the boundary layer, regulating the life cycle of sea fog. The turbulence process directly determined the maintenance and dissipation of the sea fog system. The long-distance transport of dust to the ocean and its exchange process at the air-sea interface have an important impact on the mechanism of sea fog formation and dissipation. This result supplements the impact of dust aerosols on the mechanism of sea fog formation and dissipation. It has practical reference significance for the in-depth understanding of the mechanism of sea fog formation and dissipation under complex aerosol backgrounds.

Data availability

The satellite data of H-9 is available at https://www.eorc.jaxa.jp/ptree/index.html.

The ERA5 reanalysis data is available at https://cds.climate.copernicus.eu/.

The relevant data of the observation platforms at the observation sites in this study is available at https://doi.org/10.5281/zenodo.19047355 (Ma, 2026).

https://doi.org/10.5194/egusphere-2026-1054
Preprint. Discussion started: 4 May 2026

Author contributions

Xirui Ma: Writing-original draft, Software, Data curation. Yun Zhang: Writing-review & editing, Funding acquisition. Panyan Ge: Data curation, Validation. Yan Yin: review & editing, Supervision. Hepeng Zheng: Supervision, Funding acquisition. Tingting Kang and Lingbing Bu: Supervision. Wenjie Su, Donglin Yang, Qiangyue Xiang, and Yinze Ran: Validation.

Competing interests

The authors in this article declare that they have no conflict of interest with others.

Acknowledgements

We thank the anonymous reviewers and editors for their instructive suggestions and comments.

Financial support

This study was supported by the National Natural Science Foundation of China (NSFC) (Grants 42530611, U2542209, and 42505094) and Hunan Provincial Key Research and Development Program (Project No. 2025AQ2012).

References

Bellouin, N., Quaas, J., Gryspeerdt, E., Kinne, S., Stier, P., Watson-Parris, D., Boucher, O., Carslaw, K. S., Christensen, M., Da-niau, A.-L., Dufresne, J.-L., and Feingold, G.: Bounding global aerosol radiative forcing of climate change, Rev. Geophys., 58, e2019RG000660, https://doi.org/10.1029/2019RG000660, 2020.

Bessho, K., Date, K., Hayashi, M., Ikeda, A., Imai, T., Inoue, H., Kumagai, Y., Miyakawa, T., Murata, H., Ohno, T., Okuyama, A., Oyama, R., Sasaki, Y., Shimazu, Y., Shimoji, K., Sumida, Y., Suzuki, M., Taniguchi, H., Tsuchiyama, H., Uesawa, D., Yokota, H., and Yoshida, R.: An introduction to Himawari-8/9-Japan's new-generation geostationary meteorological satellites, J. Meteorol. Soc. Jpn., 94(2), 151-183, https://doi.org/10.2151/jmsj.2016-009, 2016.

Biswas, K.F., Ghauri, B.M., and Husain, L.: Gaseous and aerosol pollutants during fog and clear episodes in South Asian urban atmosphere, Atmos. Environ., 42, 7775-7785, https://doi.org/10.1016/j.atmosenv.2008.04.056, 2008.

Boutle, I., Price, J., Kudzotsa, I., Kokkola, H., and Romakkaniemi, S.: Aerosol–fog interaction and the transition to well-mixed radiation fog, Atmos. Chem. Phys., 18, 7827-7840, https://doi.org/10.5194/acp-18-7827-2018, 2018.

https://doi.org/10.5194/egusphere-2026-1054
Preprint. Discussion started: 4 May 2026

Brege, M., Paglione, M., Gilardoni, S., Decesari, S., Facchini, M.C., Mazzoleni, L.R.: Molecular insights on aging and aqueous-phase processing from ambient biomass burning emissions-influenced Po Valley fog and aerosol, Atmos. Chem. Phys., 18, 13197–13214, https://doi.org/10.5194/acp-18-13197-2018, 2018.

Cahill, C. F.: Asian aerosol transport to Alaska during ACE-Asia, J. Geophys. Res., 108(D23), 8664, https://doi:10.1029/2002JD003271, 2003.

Clarke, A. D., Shinozuka, Y., Kapustin, V. N., Howell, S., Huebert, B., Doherty, S., Anderson, T., Covert, D., Anderson, J., Hua, X., Moore, K. G., McNaughton, C., Carmichael, G., and Weber, R.: Size distributions and mixtures of dust and black carbon aerosol in Asian outflow: Physiochemistry and optical properties, J. Geophys. Res., 109(D15), D15S09, https://doi.org/10.1029/2003JD004378, 2004.

Cotton, W. R., Bryan, G., and van den Heever, S. C.: Fogs and Stratocumulus Clouds. International Geophysics, 99(C), 179-242. https://doi.org/10.1016/S0074-6142(10)09912-2, 2011.

De Graaf, M., Schulte, R., Peers, F., Waquet, F., Tilstra, L. G., and Stammes, P.: Comparison of south-east Atlantic aerosol direct radiative effect over clouds from SCIAMACHY, POLDER and OMI–MODIS, Atmos. Chem. Phys., 20, 6707-6723, https://doi.org/10.5194/acp-20-6707-2020, 2020.

Deaconu, L. T., Ferlay, N., Waquet, F., Peers, F., Thieuleux, F., and Goloub, P.: Satellite inference of water vapour and above-cloud aerosol combined effect on radiative budget and cloud-top processes in the southeastern Atlantic Ocean, Atmos. Chem. Phys., 19, 11613-11634, https://doi.org/10.5194/acp-19-11613-2019, 2019.

Dorman, C. E., Hoch, S. W., & Gultepe, I., Wang, Q., Yamaguchi, R. T., Fernando, H. J. S. and Krishnamurthy, R.: Large-Scale Synoptic Systems and Fog During the C-FOG Field Experiment, Bound. Lay. Meteorol., 181(2), 171-202. https://doi.org/10.1007/s10546-021-00641-1, 2021.

Duce, R. A., Unni, C. K., Ray, B. J., Prospero, J. M., and Merrill, J. T.: Long-range atmospheric transport of soil dust from Asia to the tropical north pacific: temporal variability, Science., 209 (4464), 1522-1524, https://doi.org/10.1126/science.209.4464.1522, 1980.

Dusek, U., Frank, G. P., Hildebrandt, L., Curtius, J., Schneider, J., Walter, S., Chand, D., Drewnick, F., Hings, S., Jung, D., Bor-rmann, S., and Andreae, M. O.: Size Matters More Than Chemistry for Cloud-Nucleating Ability of Aerosol Particles, Science, 312, 1375-1378, https://doi.org/10.1126/science.1125261, 2006.

Fan, J., Wang, Y., Rosenfeld, D., and Liu, X.: Review of Aerosol-Cloud Interactions: Mechanisms, Significance, and Challenges, J. Atmos. Sci., 73, 4221-4252, https://doi.org/10.1175/jas-d-16-0037.1, 2016.

Fernando, H. J. S., Gultepe, I., Dorman, C. E., Pardyjak, E. R., Wang, Q., Hoch, S. W., Richter, D., Creegan, E., Gaberšek, S., Bullock, T., Wuan, M., and Wang, S.: C-FOG: Life of Coastal Fog, B. Am. Meteorol. Soc., 102, E244–E272, https://doi.org/10.1175/BAMS-D-19-0070.1, 2021.

Fernando, H. J. S., Gultepe, I., Dorman, C., Pardyjak, E., Wang, Q., Hoch, S. W., Richter, D., Creegan, E., Gaberšek, S., Bullock, T., Hocut, C., Chang, R., Alappattu, D., Dimitrova, R., Flagg, D., Grachev, A., Krishnamurthy, R., Singh, D. K., Lozovatsky, I., Nagare, B., Sharma, A., Wagh, S., Wainwright, C., Wroblewski, M., Yamaguchi, R., Bardoel, S.,

https://doi.org/10.5194/egusphere-2026-1054
Preprint. Discussion started: 4 May 2026

Coppersmith, R. S., Chisholm, N., Gonzalez, E., Gunawardena, N., Hyde, O., Morrison, T., Ol-son, A., Perelet, A., Perrie, W., Wang, S., and Wauer, B.: C-FOG: Life of Coastal Fog, B. Am. Meteorol. Soc., 102, E244-E272, https://doi.org/10.1175/bams-d-19-0070.1, 2021.

Fitzjarrald, D. R. and Lala, G. G.: Hudson Val-ley Fog Environments, J. Appl. Meteorol. Clim., 28, 1303-1328, https://doi.org/10.1175/1520-0450(1989)028<1303:hvfe>2.0.co;2, 1989.

Gilson, G.F., Jiskoot, H., Cassano, J.J., Gultepe, I., and James, T. D.: The thermodynamic structure of arctic coastal fog occurring during the melt season over East Greenland. Bound-Lay. Meteorol., 168, 443-467, https://doi.org/10.1007/s10546-018-0357-3, 2018.

Gultepe, I., Kuhn, T., Pavolonis, M., Calvert, C., Gurka, J., Heyms-field, A. J., Liu, P. S. K., Zhou, B., Ware, R., Ferrier, B., Mil-brandt, J., and Bernstein, B.: Ice Fog in Arctic During FRAM–Ice Fog Project: Aviation and Nowcasting Applications, B. Am. Meteorol. Soc., 95, 211-226, https://doi.org/10.1175/bams-d-11-00071.1, 2014.

Gultepe, I., Tardif, R., Michaelides, S.C., Cermak, J., Bott, A., Bendix, J., Müller, M.D., Pagowski, M., Hansen, B., Ellrod, G., Jacobs, W., Toth, G., and Cober, S.G.: Fog research: a review of past achievements and future perspectives, Pure Appl. Geophys, 164, 1121-1159, https://doi.org/10.1007/s00024-007-0211-x, 2007.

Gultepe, I., Zhou, B., Milbrandt, J., Bott, A., Li, Y., Heyms-field, A. J., Ferrier, B., Ware, R., Pavolonis, M., Kuhn, T., Gurka, J., Liu, P., and Cermak, J.: A review on ice fog measurements and modeling, Atmos. Res., 151, 2-19, https://doi.org/10.1016/j.atmosres.2014.04.014, 2015.

Guo, J., Liu, H., Li, Z., Rosenfeld, D., Jiang, M., Xu, W., Jiang, J. H., He, J., Chen, D., Min, M., and Zhai, P.: Aerosol-induced changes in the vertical structure of precipitation: a perspective of TRMM precipitation radar, Atmos. Chem. Phys., 18, 13329–13343, https://doi.org/10.5194/acp-18-13329-2018, 2018.

Haeffelin, M., Bergot, T., Elias, T., Tardif, R., Carrer, D., Chazette, P., Colomb, M., Drobinski, P., Dupont, E., Dupont, J.C., Gomes, L., Musson-Genon, L., Pietras, C., Plana-Fattori, A., Protat, A., Rangognio, J., Raut, J. C., Rémy, S., Richard, D., Sciare, J., and Zhang, X.: Parisfog: Shedding new Light on Fog Physical Processes, B. Am. Meteorol. Soc., 91, 767-783, https://doi.org/10.1175/2009bams2671.1, 2010.

Holets, S. and Swanson, R. N.: High-Inversion Fog Episodes in Central California, J. Appl. Meteorol. Clim., 20, 890-899, https://doi.org/10.1175/1520-0450(1981)020<0890:hifeic>2.0.co;2, 1981.

Huang, J., Wang, T., Wang, W., Li, Z., and Yan, H.: Cli-mate effects of dust aerosols over East Asian arid and semi-arid regions, J. Geophys. Res.-Atmos., 119, 11398-11416, https://doi.org/10.1002/2014JD021796, 2014.

Jia, X., Quan, J., Zheng, Z., Liu, X., Liu, Q., He, H., and Liu, Y.: Impacts of Anthropogenic Aerosols on Fog in North China Plain, J. Geophys. Res. Atmos., 124, 252-265, https://doi.org/10.1029/2018jd029437, 2019.

Kim, SH., Suh, MS., and Han, JH.: Development of Fog Detection Algorithm during Nighttime Using Himawari-8/AHI Satellite and Ground Observation Data, Asia-Pac. J. Atmos. Sci., 55, 337-350, https://doi.org/10.1007/s13143-018-0093-0, 2019.

https://doi.org/10.5194/egusphere-2026-1054
Preprint. Discussion started: 4 May 2026

Korhonen, H., Napari, I., Timmreck, C., Vehkamaki, H., Pirjola, L., Lehtinen, K. E. J., Lauri, A., and Kulmala, M.: Heterogeneous nucleation as a potential sulphate-coating mechanism of atmo-spheric mineral dust particles and implications of coated dust on new particle formation, J. Geophys. Res., 108(D17), 4546, https://doi.org/ 10.1029/2003JD003553, 2003.

Lee, Z., and Shang, S.: Visibility: How Applicable is the Century-Old Koschmieder Model?, J. Atmos. Sci., 73, 4573-4581, https://doi.org/10.1175/JAS-D-16-0102.1, 2016.

Li, W., Ito, A., Wang, G., Zhi, M., Xu, L., Yuan, Q., Zhang, J., Liu, L., Wu, F., Laskin, A., Zhang, D., Zhang, X., Zhu, T., Chen, J., Mihalopoulos, N., Bougiatioti, A., Kanakidou, M., Wang, G., Hu, H., Zhao, Y., and Shi, Z.: Aqueous-phase secondary organic aerosol formation on mineral dust, Natl. Sci. Rev., 12(7), nwaf221, https://doi.org/10.1093/nsr/nwaf221, 2025.

Liu, D. Y., Niu, S. J., Yang, J., Zhao, L. J., Lü, J. J., and Lu, C. S.: Summary of a 4-Year Fog Field Study in Northern Nanjing, Part 1: Fog Boundary Layer, Pure Appl. Geophys., 169, 809–819, https://doi.org/10.1007/s00024-011-0343-x, 2011.

Liu, M. and Matsui, H.: Aerosol radiative forcings induced by substantial changes in anthropogenic emissions in China from 2008 to 2016, Atmos. Chem. Phys., 21, 5965-5982, https://doi.org/10.5194/acp-21-5965-2021, 2021.

Luo, H., Dong, L., Chen, Y., Zhao, Y., Zhao, D., Huang, M., Ding, D., Liao, J., Ma, T., Hu, M., and Han, Y.: Interaction between aerosol and thermodynamic stability within the planetary boundary layer during wintertime over the North China Plain: aircraft observation and WRF-Chem simulation, Atmos. Chem. Phys., 22, 2507-2524, https://doi.org/10.5194/acp-22-2507-2022, 2022.

Lv J., Niu S., Zhang Y., and Xu F.: Evolution characteristics of the macro-/micro- structure and the boundary layer during a spring heavy sea fog episode in Donghai Island in Zhanjiang, Acta. Meteorol. Sin., 72(2): 350-365, https://doi.org/10.11676/qxxb2014.038, 2014.

Ma, Y., Brooks, S. D., Vidaurre, G., Khalizov, A. F., Wang, L., and Zhang, R.: Rapid modification of cloud-nucleating ability of aerosols by biogenic emissions, Geophys. Res. Lett., 40, 6293-6297, https://doi.org/10.1002/2013GL057895, 2013.

Ma, X.: Observation platform dataset of the observation point, Zenodo [Dataset], https://doi.org/10.5281/zenodo.19047355, 2026.

Maalick, Z., Kühn, T., Korhonen, H., Kokkola, H., Laaksonen, A., and Romakkaniemi, S.: Effect of aerosol concentration and absorbing aerosol on the radiation fog life cycle, Atmos. Environ., 133, 26-33, https://doi.org/10.1016/j.atmosenv.2016.03.018, 2016.

Martin, J. H., Coale, K. H., Johnson, K. S., Fitzwater, S. E., Gordon, R. M., Tanner, S. J., Hunter, C. N., Elrod, V. A., Nowicki, J. L., Coley, T. L., Barber, R. T., Lindley, S., Watson, A. J., Van Scoy, K., Law, C. S., Liddicoat, M. I., Ling, R., Stanton, T., Stockel, J., Collins, C., Anderson, A., Bidigare, R., Ondrusek, M., Latasa, M., Millero, F. J., Lee, K., Yao, W., Zhang, J. Z., Friederich, G., Sakamoto, C., Chavez, F., Buck, K., Kolber, Z., Greene, R., Falkowski, P., Chisholm, S. W., Hoge, F., Swift, R., Yungel, J., Turner, S., Nightingale, P., Hatton, A., Liss, P., and Tindale, N. W.: Testing the iron hypothesis in ecosystems of the equatorial Pacific Ocean, Nature., 371 (6493), 123-129, 10.1038/371123a0, 1994.

https://doi.org/10.5194/egusphere-2026-1054
Preprint. Discussion started: 4 May 2026

Mazoyer, M., Lac, C., Thouron, O., Bergot, T., Masson, V., and Musson-Genon, L.: Large eddy simulation of radiation fog: im-pact of dynamics on the fog life cycle, Atmos. Chem. Phys., 17, 13017-13035, https://doi.org/10.5194/acp-17-13017-2017, 2017.

Met Office: Handbook of Aviation Meteorology, 3rd edn., Her Majesty's Stationery Office, London, 1994.

Niu, S., Lu, C., Yu, H., Zhao, L., and Lü, J.: Fog research in China: An overview, Adv. Atmos. Sci., 27, 639-662, https://doi.org/10.1007/s00376-009-8174-8, 2010a.

Obiso, V., Gonçalves Ageitos, M., Pérez García-Pando, C., Perlwitz, J. P., Schuster, G. L., Bauer, S. E., Biagio, C. D., Formenti, P., Tsigaridis, K., and Miller, R. L.: Observationally constrained regional variations of shortwave absorption by iron oxides emphasize the cooling effect of dust, Atmos. Chem. Phys., 24(9), 5337-5367, https://doi.org/10.5194/acp-24-5337-2024, 2024.

Porson, A., Price, J., Lock, A., and Clark, P.: Radiation Fog. Part II: Large-Eddy Simulations in Very Stable Conditions, Bound. Lay. Meteorol., 139, 193-224, https://doi.org/10.1007/s10546-010-9579-8, 2011.

Price, J. D.: On the formation and development of radiation fog: An observational study, Bound. Lay. Meteorol., 172(2), 167-197, https://doi.org/10.1007/s10546-019-00444-5, 2019.

Qian, J., Liu, D., Yan, S., Cheng, M., Liao, R., Niu, S., Yan, W., Zha, S., Wang, L., and Chen, X.: Fog scavenging of particulate matters in air pollution events: Observation and simulation in the Yangtze River Delta, China, Sci. Total Environ., 876, 162728, https://doi.org/10.1016/j.scitotenv.2023.162728, 2023.

Quan, J., Liu, Y., Jia, X., Liu, L., Dou, Y., Xin, J., and Seinfeld, J. H.: Anthropogenic aerosols prolong fog lifetime in China, Environ. Res. Lett., 16, 044048, https://doi.org/10.1088/1748-9326/abef32, 2021.

Roach, W., Brown, R., Caughey, S., Garland, J., and Readings, C.: The physics of radiation fog: I–a field study, Q. J. Roy. Meteor. Soc., 102, 313–333, https://doi.org/10.1002/qj.49710243204, 1976.

Rodríguez, S. and López-Darias, J.: Extreme Saharan dust events expand northward over the Atlantic and Europe, prompting record-breaking PM10 and PM2.5 episodes, Atmos. Chem. Phys., 24(20), 12031-12053. https://doi.org/10.5194/acp-24-12031-2024, 2024.

Roth, A., Schneider, J., Klimach, T., Mertes, S., van Pinxteren, D., Herrmann, H., and Borrmann, S.: Aerosol properties, source identification, and cloud processing in orographic clouds measured by single particle mass spectrometry on a central European mountain site during HCCT-2010, Atmos. Chem. Phys., 16, 505-524, https://doi.org/10.5194/acp-16-505-2016, 2016.

Saide, P. E., Thapa, L. H., Ye, X., Pagonis, D., Campuzano-Jost, P., Guo, H., Schuneman, M. L., Jimenez, J. L., Moore, R., Wiggins, E., Winstead, E., Robinson, C., Thornhill, L., Sanchez, K., Wagner, N. L., Ahern, A., Katich, J. M., Perring, A. E., Schwarz, J. P., Lyu, M., Holmes, C. D., Hair, J. W., Fenn, M. A., and Shingler, T. J.: Understanding the Evolution of Smoke Mass Extinction Efficiency Using Field Campaign Measurements, Geophys. Res. Lett., 49(18), e2022GL099175, https://doi.org/10.1029/2022GL099175, 2022.

https://doi.org/10.5194/egusphere-2026-1054
Preprint. Discussion started: 4 May 2026

Schaller, C., Göckede, M., and Foken, T.: Flux calculation of short turbulent events - Comparison of three methods, Atmos. Meas. Tech., 10(3), 869-880, https://doi.org/10.5194/amt-10-869, 2017.

Schroder, J. C., Hanna, S. J., Modini, R. L., Corrigan, A. L., Krei-denwies, S. M., Macdonald, A. M., Noone, K. J., Russell, L. M., Leaitch, W. R., and Bertram, A. K.: Size-resolved observations of refractory black carbon particles in cloud droplets at a marine boundary layer site, Atmos. Chem. Phys., 15, 1367-1383, https://doi.org/10.5194/acp-15-1367-2015, 2015.

Stolaki, S., Haeffelin, M., Lac, C., Dupont, J. C., Elias, T., and Masson, V.: Influence of aerosols on the life cycle of a radiation fog event. A numerical and observational study, Atmos. Res., 151, 146-161, https://doi.org/10.1016/j.atmosres.2014.04.013, 2015.

Sullivan, R. C., Guazzotti, S. A., Sodeman, D. A., and Prather, K. A.: Direct observations of the atmospheric processing of Asian mineral dust, Atmos. Chem. Phys., 7, 1213-1236, https://doi.org/10.5194/acp-7-1213-2007, 2007.

Sullivan, R. C., Moore, M. J. K., Petters, M. D., Kreidenweis, S. M., Roberts, G. C., and Prather, K. A.: Effect of chemical mixing state on the hygroscopicity and cloud nucleation properties of calcium mineral dust particles. Atmos. Chem. Phys., 9, 3303-16, https://doi.org/10.5194/acp-9-3303-2009, 2009.

Tardif, R. and Rasmussen, R. M.: Event-Based Climatology and Typology of Fog in the New York City Region, J. Appl. Mete-orol. Clim., 46, 1141-1168, https://doi.org/10.1175/JAM2516.1, 2007.

Tobo, Y., Zhang, D., Matsuki, A., and Iwasaka, Y.: Asian dust particles converted into aqueous droplets under remote marine atmospheric conditions, Proc. Natl. Acad. Sci. USA., 107(42), 17905-17910, https://doi.org/10.1073/pnas.1008235107, 2010.

Tsai, I.C., Hsieh, P.R., Cheung, H.C., and Chou, C.K.: Aerosol impacts on fog microphysics over the western side of Taiwan Strait in April from 2015 to 2017, Atmos. Environ. 262, 118523. https://doi.org/10.1016/j.atmosenv.2021.118523, 2021.

Twomey, S.: The nuclei of natural cloud formation part II: The supersaturation in natural clouds and the variation of cloud droplet concentration, Geofisica Pura e Applicata, 43, 243-249, https://doi.org/10.1007/BF01993560, 1959.

Wang, H., Liu, X., Wu, C., Lin, G., Dai, T., Goto, D., Bao, Q., Takemura, T., and Shi, G.: Larger dust cooling effect estimated from regionally dependent refractive indices, Geophys. Res. Lett., 51(9), e2023GL107647, https://doi.org/10.1029/2023GL107647, 2024.

Wang, Y., Lu, C., Niu, S., Lv, J., Jia, X., Xu, X., Xue, Y., Zhu, L., and Yan, S.: Diverse dispersion effects and parameterization of relative dispersion in urban fog in eastern China, J. Geophys. Res.-Atmos., 128, e2022JD037514, https://doi.org/10.1029/2022JD037514, 2023.

WMO/GAW: Aerosol Measurement Procedures, Guidelines and Recommendations, WMO TD No. 1178, GAW Report No. 153, World Meteorological Organization, Geneva, Switzerland, 2003.

Yan, S., Zhu, B., Huang, Y., Zhu, J., Kang, H., Lu, C., and Zhu, T.: To what extents do urbanization and air pollution affect fog?, Atmos. Chem. Phys., 20, 5559-5572, https://doi.org/10.5194/acp-20-5559-2020, 2020.

https://doi.org/10.5194/egusphere-2026-1054
Preprint. Discussion started: 4 May 2026

Yan, S., Zhu, B., Zhu, T., Shi, C., Liu, D., Kang, H., Lu, W., and Lu, C.: The Effect of Aerosols on Fog Lifetime: Observational Evidence and Model Simulations, Geophys. Res. Lett., 48, e2020GL61803, https://doi.org/10.1029/2020gl091156, 2021.

Yang, L., Ding, S., Liu, J.-W., and Zhang, S.-P.: Effects of radiative cooling on advection fog over the northwest Pacific Ocean: observations and large-eddy simulations, Atmos. Chem. Phys., 24, 6809-6824, https://doi.org/10.5194/acp-24-6809-2024, 2024.

Yang, Y., and Gao, S.: The impact of turbulent diffusion driven by fog-top cooling on sea fog development, J. Geophys. Res. Atmos., 125(4), https://doi.org/10.1029/ 2019JD031562 e2019JD031562, 2020.

Ye, X., Wu, B., and Zhang, H.: The turbulent structure and transport in fog layers observed over the Tianjin area, Atmos. Res., 153, 217-234, https://doi.org/10.1016/j.atmosres.2014.08.003, 2015.

Yin, Y. and Chen, L.: The effects of heating by transported dust layers on cloud and precipitation: a numerical study, Atmos. Chem. Phys., 7, 3497-3505, https://doi.org/10.5194/acp-7-3497-2007, 2007.

Yin, Y., Wurzler, S., Levin, Z., and Reisin, T. G.: Interactions of mineral dust particles and clouds: Effects on precipitation and cloud optical properties, J. Geophys. Res.-Atmos., 107(D23), 4724, https://doi.org/10.1029/2001JD001544, 2002.

Yun, J. and Ha, K.-J.: Physical Processes in Sea Fog Formation and Characteristics of Turbulent Air-Sea Fluxes at Socheongcho Ocean Research Station in the Yellow Sea, Front. Mar. Sci., 9, 825973, https://doi.org/10.3389/fmars.2022.825973, 2022.

Zhang, D. Z. and Iwasaka, Y.: Size change of Asian dust particles caused by sea salt interaction: Measurements in southwestern Japan, Geophys. Res. Lett., 31(15), L15102, https://doi.org/10.1029/2004GL020087, 2004.

Zhang, D. Z., Iwasaka, Y., Shi, G. Y., Zang, J. Y., Matsuki, A., and Trochkine, D.: Mixture state and size ofAsian dust particles collected at southwestern Japan in spring 2000, J. Geophys. Res. Atmos., 108(D24), 4760, https://doi.org/10.1029/2003JD003869, 2003.

Zhang, D. Z., Shi, G. Y., Iwasaka, Y., and Hu, M.: Mixture of sulfate and nitrate in coastal atmospheric aerosols: individual particle studies in Qingdao (36 degrees 04’ N, 120 degrees 21’ E), China, Atmos. Environ., 34(17), 2669-2679, 2000.

Zhao, C. and Garrett, T. J.: Effects of Arctic haze on surface cloud radiative forcing, Geophys. Res. Lett., 42, 557-564, https://doi.org/10.1002/2014GL062015, 2015.

Zhao, S., Yan, J., Lin, Q., Yao, L., Park, K., Jung, J., Chen, L., Xu, S., Sun, M., Wang, S., Yang, H., Shi, J., Zhang, M., and Sun, H.: Changes in aerosol particle composition during sea fog formation events in the sea ice regions of the Arctic Ocean, Atmos. Environ. 272, 118943, https://doi.org/10.1016/j.atmosenv.2022.118943, 2022.

Zhou, B. and Ferrier, B. S.: Asymptotic Analysis of Equilibrium in Radiation Fog, J. Appl. Meteorol. Clim., 47, 1704-1722, https://doi.org/10.1175/2007jamc1685.1, 2008.

Zhuang, G. S., Yi, Z., Duce, R. A., and Brown, P. R.: Link between iron and sulfur cycles suggested by Fe(II) in remote marine aerosol, Nature., 355 (6360), 537-539, https://doi.org/10.1038/355537a0, 1992.